

# The K2-24 planetary system revisited by CHEOPS<sup>★</sup>

V. Nascimbeni<sup>★\*</sup><sup>1</sup>, L. Borsato<sup>1</sup>, P. Leonardi<sup>2, 1, 55</sup>, S. G. Sousa<sup>3</sup>, T. G. Wilson<sup>4</sup>, A. Fortier<sup>5, 6</sup>, A. Heitzmann<sup>7</sup>, G. Mantovan<sup>2, 1</sup>, R. Luque<sup>8</sup>, T. Zingales<sup>2, 1</sup>, G. Piotto<sup>2, 1</sup>, Y. Alibert<sup>6, 5</sup>, R. Alonso<sup>10, 11</sup>, T. Bárczy<sup>12</sup>, D. Barrado Navascues<sup>13</sup>, S. C. C. Barros<sup>3, 14</sup>, W. Baumjohann<sup>15</sup>, T. Beck<sup>5</sup>, W. Benz<sup>5, 6</sup>, N. Billot<sup>7</sup>, F. Biondi<sup>16, 1</sup>, A. Brandeker<sup>17</sup>, C. Broeg<sup>5, 6</sup>, M.-D. Busch<sup>18</sup>, A. Collier Cameron<sup>19</sup>, A. C. M. Correia<sup>20</sup>, Sz. Csizmadia<sup>21</sup>, P. E. Cubillos<sup>22, 15</sup>, M. B. Davies<sup>23</sup>, M. Deleuil<sup>24</sup>, A. Deline<sup>7</sup>, L. Delrez<sup>25, 26, 27</sup>, O. D. S. Demangeon<sup>3, 14</sup>, B.-O. Demory<sup>6, 5</sup>, A. Derekas<sup>28</sup>, B. Edwards<sup>29</sup>, D. Ehrenreich<sup>7, 30</sup>, A. Erikson<sup>21</sup>, L. Fossati<sup>15</sup>, M. Fridlund<sup>31, 32</sup>, D. Gandolfi<sup>33</sup>, K. Gazeas<sup>34</sup>, M. Gillon<sup>25</sup>, M. Güdel<sup>35</sup>, M. N. Günther<sup>36</sup>, Ch. Helling<sup>15, 37</sup>, K. G. Isaak<sup>36</sup>, F. Kerschbaum<sup>35</sup>, L. L. Kiss<sup>38, 39</sup>, J. Korth<sup>40</sup>, K. W. F. Lam<sup>21</sup>, J. Laskar<sup>41</sup>, A. Lecavelier des Etangs<sup>42</sup>, A. Leleu<sup>7, 5</sup>, M. Lendl<sup>7</sup>, D. Magrin<sup>1</sup>, P. F. L. Maxted<sup>43</sup>, B. Merín<sup>44</sup>, C. Mordasini<sup>5, 6</sup>, G. Olofsson<sup>17</sup>, R. Ottensamer<sup>35</sup>, I. Pagano<sup>45</sup>, E. Pallé<sup>10, 11</sup>, G. Peter<sup>46</sup>, D. Pollacco<sup>4</sup>, D. Queloz<sup>47, 48</sup>, R. Ragazzoni<sup>1, 9</sup>, N. Rando<sup>36</sup>, H. Rauer<sup>21, 49</sup>, I. Ribas<sup>50, 51</sup>, N. C. Santos<sup>3, 14</sup>, G. Scandariato<sup>45</sup>, D. Ségransan<sup>7</sup>, A. E. Simon<sup>5, 6</sup>, A. M. S. Smith<sup>21</sup>, R. Southworth<sup>52</sup>, M. Stalport<sup>26, 25</sup>, S. Sulis<sup>24</sup>, Gy. M. Szabó<sup>28, 53</sup>, S. Udry<sup>7</sup>, B. Ulmer<sup>46</sup>, V. Van Grootel<sup>26</sup>, J. Venturini<sup>7</sup>, E. Villaver<sup>10, 11</sup>, and N. A. Walton<sup>54</sup>

(Affiliations can be found after the references)

Submitted 23 May 2024 / Accepted 4 September 2024

## ABSTRACT

The planetary system K2-24 is composed of two transiting low-density Neptunians locked in an almost perfect 2:1 resonance and showing large transit time variations (TTVs), and it is an excellent laboratory to search for signatures of planetary migration. Previous studies performed with K2, Spitzer, and RV data tentatively claimed a significant non-zero eccentricity for one or both planets, possibly high enough to challenge the scenario of pure disk migration through resonant capture. With 13 new CHEOPS light curves (seven of planet b, six of planet c), we carried out a global photometric and dynamical re-analysis by including all the available literature data as well. We obtained the most accurate set of planetary parameters to date for the K2-24 system, including radii and masses at 1% and 5% precision (now essentially limited by the uncertainty on stellar parameters) and non-zero eccentricities  $e_b = 0.0498^{+0.0011}_{-0.0018}$ ,  $e_c = 0.0282^{+0.0003}_{-0.0007}$  detected at very high significance for both planets. Such relatively large values imply the need for an additional physical mechanism of eccentricity excitation during or after the migration stage. Also, while the accuracy of the previous TTV model had drifted by up to 0.5 days at the current time, we constrained the orbital solution firmly enough to predict the forthcoming transits for the next ~15 years, thus enabling efficient follow-up with top-level facilities such as JWST or ESPRESSO.

**Key words.** Techniques: photometric – Planetary systems – Planets and satellites: detection

## 1. Introduction

The advent of space-based high-precision photometry, inaugurated by CoRoT (Auvergne et al. 2009) and then continued by Kepler (Borucki et al. 2010), its second phase K2 (Howell et al. 2014), and more recently by TESS (Ricker et al. 2015), has enabled not only the unexpected discovery of entirely new classes of exoplanets but also the application of analysis techniques hitherto relegated to theory. Among these, one of the most fruitful is a dynamical technique known as transit time variations (TTVs; Agol et al. 2005), in which the gravitational perturbation between planets and its time-variable effect on the measured orbital periods is exploited to retrieve their orbital solution. In the case where two or more planets transit their host stars, TTVs are very

effective at both confirming the planetary nature of candidates and measuring their masses without the need of (or in synergy with; Malavolta et al. 2017) radial velocity (RV) measurements.

Dynamical simulations have shown that the expected amplitude of TTVs in ordinary planetary systems is quite small, usually on the order of magnitude of seconds to minutes (Holman & Murray 2005). Such an amplitude is close or even below the detection limit imposed by photon noise and/or stellar activity (Barros et al. 2013). A fairly interesting exception is represented by systems where planets are locked in mean-motion resonances (MMRs) or, more generally, close to commensurability,<sup>1</sup> the orbital period ratio being close to an integer ratio. Low-order MMRs in the  $j + 1 : j$  form ( $j \in \mathbb{N}$ ), such as 2:1 or 3:2 can boost the TTV signal by orders of magnitude, reaching hours or even days in the most favorable configurations (Agol & Fabrycky 2018). A famous case, and the first one to be investigated,

<sup>★</sup> This article uses data from the CHEOPS program CH\_PR100025. The individual data sets are listed in Table A.1. Table 3, the light curves and the predicted transit times are only available in electronic form at the CDS: <http://cdsweb.u-strasbg.fr/cgi-bin/qcat?J/A+A/>.  
<sup>\*\*</sup> send offprint requests to: valerio.nascimbeni@inaf.it

<sup>1</sup> Being close to an integer ratio of orbital periods does not necessarily imply the system is in an MMR from a dynamical point of view; see also our discussion in Section 5.3.

is the *Kepler-9* system (Holman et al. 2010), a pair of transiting warm Saturn-sized planets orbiting their host in about 19.2 and 38.9 days, that is, close to a 2:1 MMR. Resonant configurations are not merely a useful playground to exploit the TTV technique. Rather, they are also extremely interesting by themselves since they represent a unique laboratory to test planetary formation and migration theories (Batygin 2015). In particular, how resonances can be maintained during a disk-migration phase and form or change at a later stage is currently a very active area of debate (Huang & Ormel 2023 and references therein).

The typical timescale of the orbital period modulation induced by the TTV (sometimes called the “superperiod”;  $P_{\text{TTV}}$ ) needs to be fully mapped to avoid degeneracy in the dynamical retrieval, and it can reach months or even years. In the Hadden & Lithwick (2016) approximation, the superperiod can be estimated as a function of the orbital periods of the inner and outer planets:

$$P_{\text{ttv}} = \left| \frac{j+1}{P_{\text{out}}} - \frac{j}{P_{\text{in}}} \right|^{-1}. \quad (1)$$

For most orbital configurations,  $P_{\text{TTV}}$  can be significantly longer than the average duration of a K2 campaign ( $\sim 70$ -80 days) or a TESS sector ( $\sim 27$  days). Even if TESS, by design, is able to revisit a given target throughout additional sectors (according mostly to its ecliptic latitude), the sampling of the transit times can be very sparse, especially in the long-period regime ( $P \geq 30$  d). This is particularly true for those systems discovered by K2, which lie close to the ecliptic and are therefore rarely monitored by TESS, if at all.

On the other hand, the ESA S-class mission CHEOPS (Benz et al. 2021; Fortier et al. 2024), launched in 2019, is very efficient at observing at low ecliptic latitudes, and being a single-target telescope, it has the ability to gather even very long-period transits, once their ephemeris is reasonably constrained. CHEOPS has been successfully exploited several times to follow up on systems discovered by K2, sometimes with a particular focus on TTV analysis. One such system is WASP-47 (Nascimbeni et al. 2023), for which our analysis led to an improvement of the orbital and physical parameters and, in particular, of the density of planet d. We chose K2-24 as the next system to explore for the science case mentioned above within the CHEOPS GTO program.

The system K2-24, announced by Petigura et al. (2016) (hereafter P16), is a planetary system made by two (sub-)Saturn-sized ( $R_b \simeq 5.6 R_{\oplus}$ ,  $R_c \simeq 8 R_{\oplus}$ ) planets close to a 2:1 period ratio, with orbital periods of  $P_b \simeq 21$  and  $P_c \simeq 42$  days. Since the baseline of the K2 light curve was not long enough to detect TTVs, the discovery paper had to rely on the HRES RVs alone to constrain the planetary masses, which turned out to be in the Neptunian range ( $M_b = 21.0 \pm 5.4 M_{\oplus}$ ,  $M_c = 27 \pm 7 M_{\oplus}$ ), hence making K2-24b and -c extremely inflated planets with unusually large H/He envelopes predicted by models. A further PSF/HARPS RV follow-up by Dai et al. (2016) essentially confirmed the mass estimates at  $M_b = 20 \pm 4 M_{\oplus}$  and  $M_c = 26 \pm 6 M_{\oplus}$ . The only follow-up transits published so far (two of -b and two of -c), observed by Spitzer in 2015-2016, were presented by Petigura et al. (2018) (hereafter P18), who also merged all the existing photometric and spectroscopic data and carried out the first TTV analysis of this system, revealing even smaller masses ( $M_b = 19 \pm 2 M_{\oplus}$ ,  $M_c = 15 \pm 2 M_{\oplus}$ ) and tentatively detecting the presence of an outer  $54 \pm 14 M_{\oplus}$  companion at  $\sim 1.1$  au.

The TTV modeling by P18, performed through the analytic approach developed by Lithwick et al. (2012) and based on transit data covering only  $\sim 40\%$  of  $P_{\text{TTV}}$ , did not yield a precise

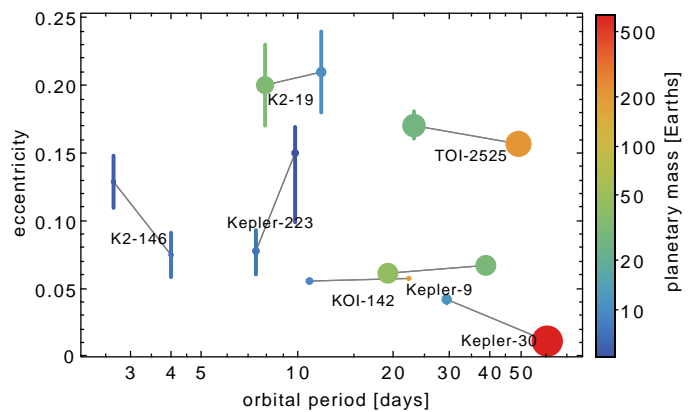


**Fig. 1.** Orbital eccentricities constrained at better than  $3\sigma$  for resonant pairs of transiting planets, from the NASA Exoplanet Archive (see text for references). Each pair is linked with a gray segment and labelled with the host star name. The point size is proportional to the planetary radius, while the planetary mass is color-coded.

measurement for both eccentricities  $e_b$  and  $e_c$ . Rather, it concluded that at least one planet must have an eccentricity significantly larger than zero, adopting  $e_b = 0.06 \pm 0.01$  and  $e_c < 0.07$  (at 90% confidence) based on dynamical stability constraints and an imposed prior derived from the distribution of  $\langle e \rangle$  observed in *Kepler* multi-planet systems. Antoniadou & Libert (2020) later presented a more detailed analysis of dynamical stability in K2-24 based on the planetary parameters by P18, concluding that MMR locking protects its long-term evolution and more tightly constraining the eccentricity of the outer planet to  $e_c < 0.05$ .

Teyssandier & Libert (2020) further investigated the dynamical architecture of K2-24 and its implications for its formation and migration history, concluding that a pure disc-induced migration is not able to reproduce the period ratio and the TTV amplitude observed and that it would result in much smaller eccentricities, by a factor of  $\sim 30$ . Rather, they proposed a two-stage scenario where the two planets are first captured in resonance at low eccentricities within the disk. Then eccentricities are excited by an outer companion (such as the one hinted at by RV observations) during the disk dispersal phase. The same authors also suggested that the actual value of  $e_b$  and  $e_c$  may be higher than the P18 estimate, according to their simulations.

Only for a handful of transiting planetary systems are there accurate eccentricities for planets in or close to low-order MMRs. From the latest version of the NASA Exoplanet Archive (Akeson et al. 2013; v. 2023-12-28), only seven<sup>2</sup> pairs of resonant<sup>3</sup> planets can be found with both eccentricities constrained at better than  $3\sigma$  (Fig. 1). Sorted by increasing average orbital period, they are K2-146 b/c (Hamann et al. 2019), *Kepler-223* b/c (Mills et al. 2016), K2-19 b/c (Petigura et al. 2020), KOI-142=*Kepler-88* b/c (Weiss et al. 2020), *Kepler-9* b/c (Borsato et al. 2019), TOI-2525 b/c (Trifonov et al. 2023), and *Kepler-30* b/c (Sanchis-Ojeda et al. 2012). Among these, only K2-146 and *Kepler-223* lie in the Neptunian mass regime but are quite close-in at  $P < 10$  d, where tidal interactions with the host star start to become significant (Lithwick & Wu 2012). From this point of view, the K2-24 system offers us the rare opportunity to probe

<sup>2</sup> An additional eighth system is TIC279401253 (Bozhilov et al. 2023), a 2:1 pair of giants ( $P_b \simeq 77$  d,  $P_c \simeq 155$  d) whose outer one is not transiting and detected through RVs.

<sup>3</sup> All the listed pairs lie in or close to the 3:2 MMR (K2-146, *Kepler-223*, K2-19) or the 2:1 MMR (all the others).

the “primordial” eccentricities of a pair of warm ( $T_{\text{eq}} < 800$  K) Neptunians (i.e., not affected by tidal effects).

The aim of this paper is to present and analyze thirteen new CHEOPS observations of K2-24-b/c and to merge them with all the existing literature light curves and RVs in order to derive an updated and consistent dynamical solution able to 1) recover the transit ephemeris for any future follow-up; 2) improve the measurement of planetary masses, radii, and densities, with a particular focus on the implications for their inner structure; and 3) firmly detect eccentricities for both planets. We present the new observations together with the employed archival data in Section 2. We describe the photometric modeling of the light curves in Section 3 and then the global TTV+RV dynamical analysis in Section 4. Finally, the results are compared and interpreted in Section 5, where prospects for the future characterization of this system are also discussed.

## 2. Observations

We collected all the available photometric and spectroscopic data of K2-24 for our analysis; they are described in the following subsections. The very long orbital periods of K2-24b and -c, together with their long duration, uncertain ephemeris (See Section 2.3), and small transit depths (2-4 mmag), make the ground-based follow-up of this system extremely difficult. Indeed, no ground-based light curves have been published so far. It is also worth mentioning that K2-24 was not observed by TESS in its first six observing cycles (2018-2024). All the time stamps of the photometric and spectroscopic data described below were uniformly converted to the BJD-TDB standard and referred to the mid-exposure instant, following the prescription by Eastman et al. (2010).

### 2.1. K2 and Spitzer photometry

K2-24 has been observed by K2 once, in Campaign 2, from 2014-08-23 to 2014-11-13. This uninterrupted,  $\sim 75$  day-long light curve contains four transits of planet -b and two transits of planet -c (plotted with green points in Fig. A.3) and led to their discovery published by P16. This light curve has been corrected for systematic errors due to the spacecraft jitter and drifting by following the approach developed by Vanderburg & Johnson (2014).

Four more transits were secured by Spitzer and presented by P18: two of planet -b on 2015-10-27 and 2016-06-13, and two of planet -c on 2015-11-12 and 2016-06-10. Both of the time series of planet c actually cover partial transits. The scheduling was based on a simple linear ephemeris since a more sophisticated TTV model was not yet available at that time. All the Spitzer light curves have been corrected for systematics through the pixel-level decorrelation algorithm (PLD; Deming et al. 2015) as modified by Benneke et al. (2017).

### 2.2. HST photometry

We downloaded the publicly available HST WFC3 G141 observations of K2-24b from the MAST archive. These data cover a single transit gathered on 2016-07-04 as part of proposal GO-14455 (PI: E. Petigura, plotted with orange points in Fig. A.3) to extract a transmission spectrum of the planetary atmosphere. These observations have been analyzed previously by Edwards et al. (2023b) – we return to their results in Section 5. The visit consists of a total of eight HST orbits. In our analysis,

we excluded the first one due to the presence of significant time-dependent systematic errors. At the beginning of each orbit, a direct image captured with the F130N filter was used for wavelength calibration. These data were collected with the GRISM256 aperture and the SPARS10 reading sequence. The total exposure time was set to 103.13 s, with 16 up-the-ramp reads for exposure. Both scanning directions were employed.

We calibrated the raw WFC3 data and extracted the photometric information through the IRACLIS dedicated pipeline (Tsiaras et al. 2016a, 2016b, 2018). We extracted the detrended white-light curve (spectral range: 1.088 to 1.680  $\mu\text{m}$ ; plotted with orange points in Fig. A.3) from the calibrated images, taking into account the tilted configuration of the WFC3/NIR detector and modeling the time-dependent systematics using the Eq. 1 of Edwards et al. (2023a). The HST WFC3 time series are often affected by linear long-term and exponential short-term (“orbit ramps”) trends, especially when observing bright sources. We note that both ingress and egress are missing from this visit, implying that the transit time  $T_0$  is expected to be relatively poorly constrained.

### 2.3. CHEOPS photometry

K2-24 was targeted by CHEOPS thirteen times over a span of about two years within the GTO subprogram #25 (PID PR100025) focused on the study of the mass-radius relation through the TTV analysis of resonant pairs of low-mass exoplanets. A complete log of the observations is reported in Table A.1. The corresponding light curves, extracted by the CHEOPS DRP v14 pipeline (Hoyer et al. 2020), are plotted in Fig. 2 and labelled with matching IDs. The gaps located at regular time intervals are due to the avoidance angles of CHEOPS and to the SAA crossing events, Earth occultations, and Earth stray light contamination during its 98.77-min low Earth orbit.

It is evident that, particularly for planet c, some transits are partial ones. This is due to the transit predictions by P18 becoming increasingly inaccurate as the time passed since the K2/Spitzer observations increased. The  $O - C$  (observed minus calculated) discrepancy is much larger than the prediction errors reported in Table 4 of P18, demonstrating that their dynamical solution had to be revised and improved in order to reliably predict the future transit times.

### 2.4. Radial velocities

The merged data set we collected is made of 89 RV observations in total from three different instruments, including 63 RV points from HIRES, published by P18 (the first 32 having already been analyzed by P16); 16 RV points from PFS, presented by Dai et al. (2016); ten RV points from HARPS (PID: 095.C-0718), also presented by Dai et al. (2016). Two additional HARPS points can be found in the ESO archive (PID: 191.C-0873), but we did not include them in our analysis since they are affected by an RV offset introduced on 2015-06-03. We emphasize that our goal in this work was to fit all of these RV data simultaneously for the first time, as P18 did not include the PFS and HARPS data in their modeling.

## 3. Light curve modeling

We performed global modeling of our 13 CHEOPS, six K2, and one HST light curves by simultaneously fitting the signal of

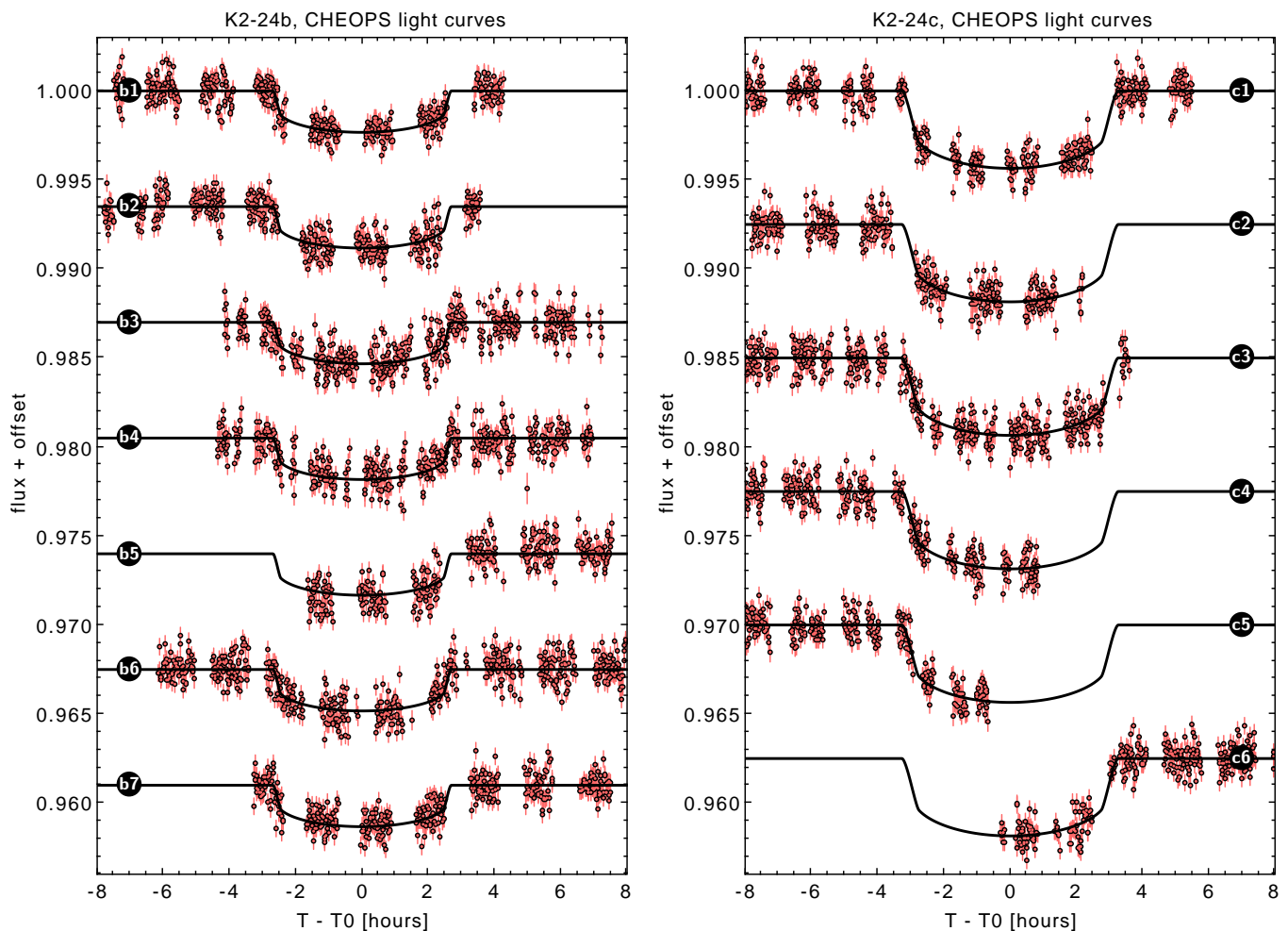


**Fig. 2.** Light curves of K2-24b (left panel) and K2-24c (right panel) from CHEOPS analyzed for the present work, after detrending. For each light curve, the corresponding label matches the ID given in Table A.1. Arbitrary vertical offsets of 0.065 and 0.0075 were added, respectively, to both sets for visualization purposes.

planet -b and -c on both data sets, using the PyORBIT<sup>4</sup> software version 10 (Malavolta et al. 2016, 2018). After some preliminary tests, we decided not to incorporate the Spitzer light curves into our global fit, as their transit depths are clearly inconsistent with the K2, CHEOPS, and HST data, and also with each other. This could be due to an imperfect correction of systematic errors since the transits are partial and the detrending process works by extrapolation rather than interpolation. To avoid any bias in our retrieved planetary parameters, we took the transit times  $T_0$  for our dynamical analysis (Section 4) from Table 1 of P18 instead.

The K2, CHEOPS, and HST transits were modeled with the Batman code (Kreidberg 2015) and parametrized as a function of the impact parameter  $b$ , the radius ratio  $R_p/R_*$ , and the scaled semi-major axis  $a/R_*$ . The transit model for K2 was super-sampled by a factor of ten to account for the non-negligible length of the K2 exposure times (30-minute cadence). Each transit time  $T_0$  (13 from CHEOPS, six from K2, one from HST) was treated as a free, independent parameter, so the orbital period  $P$  was fixed at its average value interpolated over our observations, that is,  $P_b = 20.8891$  and  $P_c = 42.3391$  days. The limb darkening effect was modeled through a quadratic law with two parameters called  $u_1$  and  $u_2$  for each instrument. Internally,  $u_1$  and  $u_2$  were re-parametrized as  $q_1$  and  $q_2$  following the prescrip-

tion by Kipping (2013) to minimize the correlation between the two parameters.

The residual systematic errors present in the CHEOPS light curves  $f(t)$  were detrended as a linear combination of terms as a function of external parameters: the first and second-order derivative of the centroid offset in  $x$  and  $y$  pixel coordinates ( $df/dx$ ,  $d^2f/dx^2$ ,  $df/dy$ ,  $d^2f/dy^2$ ), background level ( $df/db$ ), photometric contamination factor ( $df/dcontam$ ), the first three harmonics of the spacecraft roll angle (in  $\cos \phi$  and  $\sin \phi$ ), and a quadratic baseline  $f_0 + df/dt + d^2f/dt^2$ . The roll angle term, as expected with data from a low Earth orbit satellite, always dominates. Since adding 15 free parameters for each CHEOPS data set would have implied  $13 \times 15 = 195$  free parameters in our global fit just for the detrending (which is prohibitively expensive in terms of computational time), we went through the two-stage approach described in Nascimbeni et al. (2023). In a first pass, each individual CHEOPS light curve was fitted with both a transit model and the detrending model. Then the detrended light curves were fed into the final global fitting. The latter therefore had 52 free parameters: six LD coefficients ( $u_1$  and  $u_2$  for CHEOPS, K2, HST), six planetary parameters ( $b$ ,  $R_p/R_*$ ,  $a/R_*$  for -b and -c), 20 transit times, and 20 jitter parameters (one for each light curve).

We set uninformative priors on all our fitting parameters. The only exceptions are the six limb darkening parameters  $u_1$ ,

<sup>4</sup> <https://github.com/LucaMalavolta/PyORBIT>

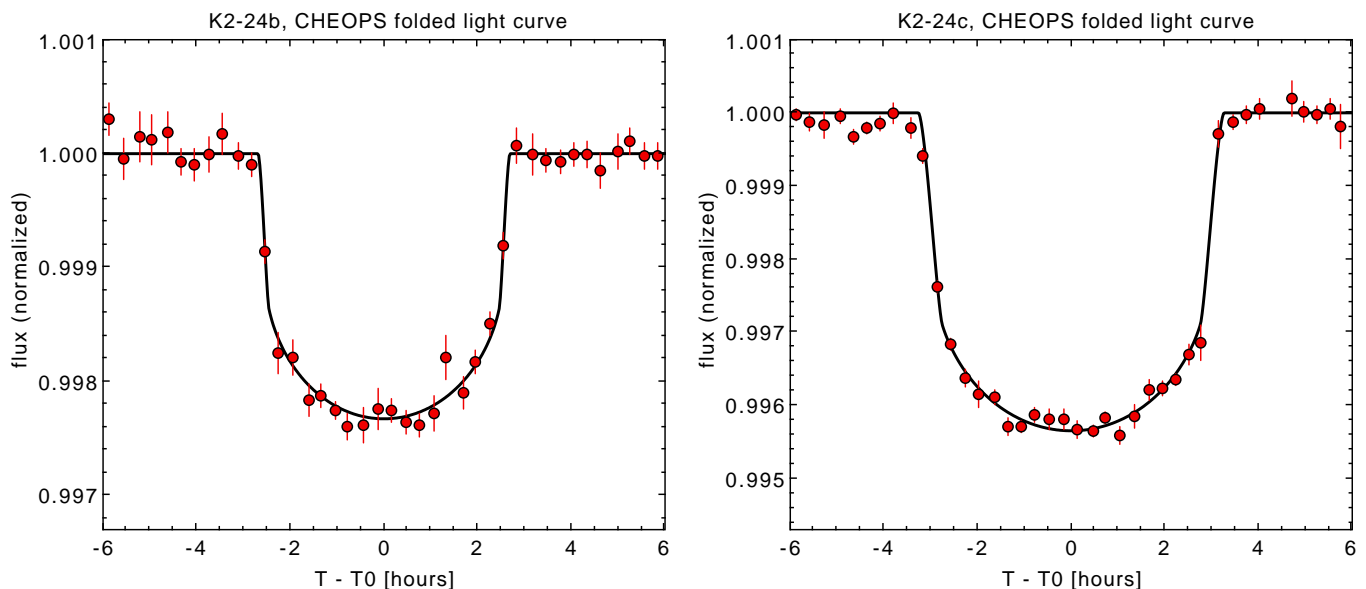


**Fig. 3.** Folded light curves of K2-24b (left panel) and K2-24c (right panel) from CHEOPS, binned over 0.3-hour intervals.

**Table 1.** Stellar parameters of K2-24 adopted for our analysis.

Parameter [unit]	value	source
distance [pc]	$170.5 \pm 0.5$	<i>Gaia</i> DR3
$T_{\text{eff}}$ [K]	$5726 \pm 65$	TS3
$\log g$ [cgs]	$4.48 \pm 0.03$	TS3
[Fe/H]	$0.41 \pm 0.05$	TS3
age [Gyr]	$4.9 \pm 1.7$	TS3
$v \sin i$ [km/s]	$< 2$	TS3
$v_{\text{mic}}$ [km/s]	$1.09 \pm 0.03$	TS3
$R_{\star}$ [ $R_{\odot}$ ]	$1.185 \pm 0.011$	TS3
$M_{\star}$ [ $M_{\odot}$ ]	$1.091 \pm 0.056$	TS3

**Notes.** Sources: *Gaia* DR3 (Gaia Collaboration et al. 2023), CHEOPS working group TS3 (see Borsato et al. 2021, Section 3.2.1 for details)

$u_2$  for CHEOPS, K2, and HST. We carried out two independent analyses: the first one with fully uninformative priors (LD-free) and a second one by centering the prior at the theoretical value computed by the LDTk code (Parviainen & Aigrain 2015) and increasing to 0.05 the associated Gaussian error in order to accommodate for the well-known underestimation by models (LD-prior). The input stellar parameters were computed by the CHEOPS Target Characterization (TS3) working group according to the procedure described by Borsato et al. (2021), Section 3.2.1, and reported in Table 1. We set PyORBIT to use PyDE (Parviainen et al. 2016) to find a reasonable starting point in the parameter space (50 000 generations with a population size of  $8 \times N_{\text{par}}$ , where  $N_{\text{par}}$  is the number of free parameters). Then we initialized an Markov chain Monte Carlo (MCMC) optimization with emcee (Foreman-Mackey et al. 2013), running for 500 000 steps and setting a thinning factor of 100. After discarding the first 50 000 steps as the burn-in phase, convergence was checked by auto-correlation function analysis (ACF).

All the final best-fit parameters of interest from the MCMC distributions are reported in Table 2 for both the “LD-free” and “LD-prior” case; transit times are reported separately in Table 3. The corresponding corner plots for the transit shape param-

eters (i.e., excluding transit times, LD, and jitter parameters) are shown in Fig. A.1 and Fig. A.2. The best-fit values of  $u_1$  and  $u_2$  are consistent between the LD-free and LD-prior case (Table 2), although of course LD-prior has smaller error bars; all the remaining parameters agree within  $1 \sigma$ . We adopt the LD-prior solution throughout the following analysis. We plot the CHEOPS light curves of K2-24b and -c folded on the best-fit individual  $T_0$  and binned over 0.3-hour intervals in Fig. 3.

In the last column of Table 2 we also compare our results with the literature, namely with P16 (P18 did not present a new set of independent planetary parameters since the work was based on priors from P16). Overall there is very good agreement. The planetary radii  $R_b$  and  $R_c$ , in particular, are consistent within  $1 \sigma$ , but our error bars are improved by an order of magnitude (i.e., from a relative error of  $\sim 9\%$  to  $\sim 1\%$ ). The uncertainty is now limited by our current knowledge of the stellar radius  $\sigma(R_{\star})/R_{\star} \simeq 1\%$  (Table 1).

## 4. Dynamical modeling

We carried out a dynamical modeling of the K2-24 system and its strong TTV signals by simultaneously fitting the three RV data sets available (see Section 2.4) and the transit times ( $T_{0s}$ ) extracted with PyORBIT (see Table 3) through the TRADES code<sup>5</sup> (Borsato et al. 2014, 2019, 2021). We adopted a parameterization similar to Nascimbeni et al. (2023), assuming a three-planet<sup>6</sup> model and fitting for the stellar mass  $M_{\star}$ , planetary-to-star mass ratio  $M_p/M_{\star}$ , periods  $P$ , mean longitude<sup>7</sup>  $\lambda$  of all planets, eccentricity  $e$ , and argument of periastron passage  $\omega$  in the form  $\sqrt{e} \cos \omega$  and  $\sqrt{e} \sin \omega$  for planets -b and -c (as specified by the indexes  $b$  and  $c$ ). We also fit a jitter term in  $\log_2$ -space, and an offset for each RV data set. We fixed the following param-

<sup>5</sup> <https://github.com/lucaborsato/trades>

<sup>6</sup> Candidate planet d (at  $\simeq 1.1$  au) is far enough to be dynamically decoupled from the inner pair, so in principle it should not impact the TTV signals. It has to be included in our dynamical modeling, though, because of its effect on RV, as in P18.

<sup>7</sup> The mean longitude is defined as  $\lambda = \mathcal{M} + \Omega + \omega$ , where  $\mathcal{M}$  is the mean anomaly,  $\Omega$  is the longitude of ascending node, and  $\omega$  is the argument of pericenter.

**Table 2.** Posterior and derived parameters of the K2-24 system from the global PyORBIT fit on the K2+HST+CHEOPS data set.

Parameter [unit]	<i>LD-prior</i> <sup>†</sup> (adopted)		<i>LD-free</i> <sup>†</sup>		Literature
	MAP (HDI±1σ)	Prior	MAP (HDI±1σ)	Prior	P16
<i>Planet K2-24b</i>					
$a/R_\star$	$30.38^{+0.53}_{-1.00}$	$\mathcal{U}(20, 40)$	$30.18^{+0.73}_{-1.30}$	$\mathcal{U}(20, 40)$	$28.6^{+1.7}_{-3.6}$
$R_p/R_\star$	$0.04356^{+0.00034}_{-0.00021}$	$\mathcal{U}(0.0, 0.1)$	$0.04368^{+0.00049}_{-0.00030}$	$\mathcal{U}(0.0, 0.1)$	$0.0431^{+0.0017}_{-0.0008}$
$b$	$0.20^{+0.12}_{-0.13}$	$\mathcal{U}(0, 1)$	$0.24^{+0.13}_{-0.15}$	$\mathcal{U}(0, 1)$	$0.37^{+0.22}_{-0.24}$
$i$ [deg]	$89.63^{+0.25}_{-0.25}$	(derived)	$89.55^{+0.30}_{-0.28}$	(derived)	$89.25^{+0.49}_{-0.61}$
$R_p/R_\oplus$	$5.638^{+0.065}_{-0.061}$	(derived)	$5.655^{+0.076}_{-0.069}$	(derived)	$5.68 \pm 0.56$
$T_{14}$ [days]	$0.22437^{+0.00086}_{-0.00075}$	(derived)	$0.22419^{+0.00099}_{-0.00083}$	(derived)	$0.2283^{+0.0029}_{-0.0017}$
$T_{23}$ [days]	$0.20470^{+0.00078}_{-0.00094}$	(derived)	$0.2042^{+0.0010}_{-0.0013}$	(derived)	$0.2062^{+0.0020}_{-0.0046}$
$a$ [au]	$0.1673^{+0.0034}_{-0.0056}$	(derived)	$0.1662^{+0.0043}_{-0.0071}$	(derived)	$0.154 \pm 0.002$
<i>Planet K2-24c</i>					
$a/R_\star$	$47.6^{+2.4}_{-2.0}$	$\mathcal{U}(30, 60)$	$46.9^{+2.1}_{-1.7}$	$\mathcal{U}(30, 60)$	$52.6^{+0.0}_{-2.6}$
$R_p/R_\star$	$0.06133^{+0.00068}_{-0.00080}$	$\mathcal{U}(0.0, 0.1)$	$0.06171^{+0.00068}_{-0.00080}$	$\mathcal{U}(0.0, 0.1)$	$0.0594^{+0.0010}_{-0.0004}$
$b$	$0.462^{+0.066}_{-0.100}$	$\mathcal{U}(0, 1)$	$0.489^{+0.056}_{-0.083}$	$\mathcal{U}(0, 1)$	$0.22^{+0.17}_{-0.16}$
$i$ [deg]	$89.44^{+0.15}_{-0.11}$	(derived)	$89.40^{+0.12}_{-0.10}$	(derived)	$89.76^{+0.18}_{-0.21}$
$R_p/R_\oplus$	$7.93^{+0.12}_{-0.13}$	(derived)	$7.98^{+0.12}_{-0.13}$	(derived)	$7.82 \pm 0.72$
$T_{14}$ [days]	$0.2707^{+0.0018}_{-0.0018}$	(derived)	$0.2708^{+0.0016}_{-0.0016}$	(derived)	$0.2696^{+0.0017}_{-0.0013}$
$T_{23}$ [days]	$0.2315^{+0.0026}_{-0.0025}$	(derived)	$0.2301^{+0.0028}_{-0.0025}$	(derived)	$0.2375^{+0.0013}_{-0.0025}$
$a$ [au]	$0.262^{+0.014}_{-0.011}$	(derived)	$0.258^{+0.012}_{-0.010}$	(derived)	$0.247 \pm 0.004$
<i>Limb darkening parameters</i>					
$u_1$ (K2, linear)	$0.527^{+0.025}_{-0.025}$	$\mathcal{N}(0.55, 0.05)$	$0.561^{+0.065}_{-0.063}$	$\mathcal{U}(0.0, 1.0)$	$0.568 \pm 0.003$
$u_2$ (K2, quadratic)	$0.043^{+0.040}_{-0.039}$	$\mathcal{N}(0.05, 0.05)$	$-0.02^{+0.11}_{-0.10}$	$\mathcal{U}(-0.5, 0.5)$	$0.098 \pm 0.005$
$u_1$ (HST, linear)	$0.196^{+0.035}_{-0.036}$	$\mathcal{N}(0.24, 0.05)$	$0.103^{+0.098}_{-0.070}$	$\mathcal{U}(0.0, 1.0)$	$0.568 \pm 0.003$
$u_2$ (HST, quadratic)	$0.147^{+0.046}_{-0.046}$	$\mathcal{N}(0.16, 0.05)$	$0.24^{+0.16}_{-0.20}$	$\mathcal{U}(-0.5, 0.5)$	$0.098 \pm 0.005$
$u_1$ (CHEOPS, linear)	$0.562^{+0.030}_{-0.030}$	$\mathcal{N}(0.55, 0.05)$	$0.652^{+0.092}_{-0.097}$	$\mathcal{U}(0.0, 1.0)$	—
$u_2$ (CHEOPS, quadratic)	$0.035^{+0.041}_{-0.041}$	$\mathcal{N}(0.06, 0.05)$	$-0.11^{+0.15}_{-0.13}$	$\mathcal{U}(-0.5, 0.5)$	—

**Notes.** The columns give the parameter name and unit (where applicable); the MAP value of the posterior distribution; its 1- $\sigma$  HDI and the adopted prior for the LD-prior and LD-free case, respectively (<sup>†</sup> see Section 3 for details); and the best-fit values from the literature (P16), for comparison.

eters: longitude of ascending node  $\Omega$  to  $180^\circ$  for each planet; circular orbit of planet d (eccentricity  $e_d = 0$  and argument of periastron  $\omega_d = 90^\circ$ ); and inclination,  $i$ , of planets -b and -c as in Table 2 and to  $90^\circ$  for planet d. All the parameters are defined at the reference time  $T_{\text{ref}} = 2456905 \text{ BJD}_{\text{TDB}}$ . We defined the parameter priors in the physical space and converted them into fitting space; all the priors used are reported in Table 4.

We first ran TRADES with PyDE (100 different configurations for 150 000 generations) to find a suitable starting point. Then, we ran EMCEE with 100 walkers for 1 000 000 steps, and we applied a conservative thinning factor of 100. As in Nascimbeni et al. (2023), we used a combination of the differential evolution proposal (80% of the walkers; Nelson et al. 2014) and the snooker differential evolution proposal (20% of the walkers; ter Braak & Vrugt 2008) as the sampler within EMCEE. After checking the chains' convergence through Gelman-Rubin statistics (Gelman & Rubin 1992), Geweke criterion (Geweke 1991), ACF, and visual inspections, we discarded as burn-in the first 50% of the steps. From the posterior distributions, we extracted the maximum a posteriori (MAP<sup>8</sup>) as the best-fit parameters and

<sup>8</sup> By MAP we mean the set of parameters that maximize the log-probability of the posterior distributions. If all the priors were uninfor-

the uncertainties as the high density interval (HDI) at 68.27%.<sup>9</sup> The best-fit parameters from TRADES and their uncertainties are reported in Table 4, with a comparison with P18 for the parameters in common. The TTV and RV models from the best-fit orbital solution by TRADES were also plotted along with the observed data points in Fig. 4 and Fig. 5, respectively. The fit looks perfectly satisfactory, with an overall reduced  $\chi^2$  (TTV+RV) of 1.33 with 94 degrees of freedom. The corresponding  $\ln \mathcal{L}$  and  $\ln(\text{probability})$  values are  $-107.242$  and  $-107.623$ , respectively.

A useful application of our dynamical model is the prediction of future transit events for any follow-up opportunity. As for planets -b and c, transits cannot be reliably scheduled according to a linear ephemeris. The combined impact of a poorly constrained linear ephemeris with a set of orbital parameters determined over a relatively short time span has been discussed in Borsato et al. (2022) in the context of the scientific preparation of the Ariel mission (Tinetti et al. 2018).

All the transits of planets -b and -c predicted by our best-fit dynamical model up to and including the year 2029 are re-

mative and uniform, then the MAP would correspond to the maximum likelihood estimation (MLE).

<sup>9</sup> An HDI at 68.27% is equivalent to the 16<sup>th</sup>-84<sup>th</sup> percentiles of a Gaussian distribution.

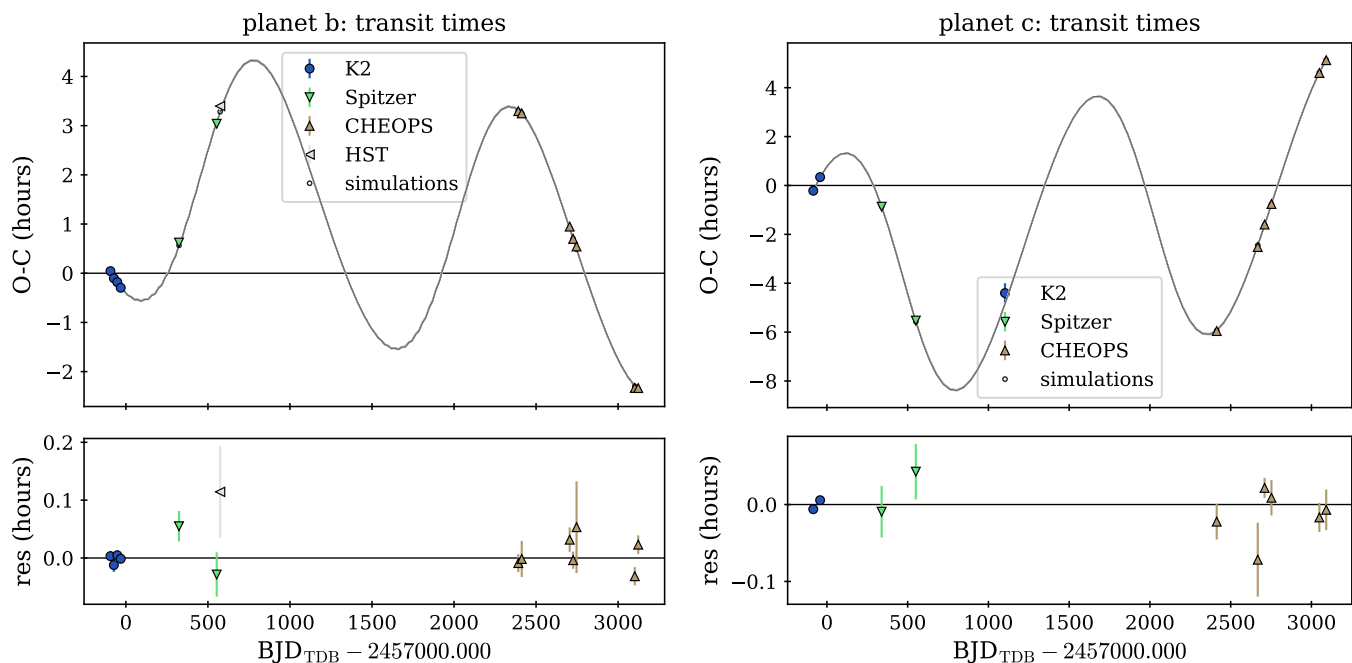


**Fig. 4.** TTV modeling of K2-24b (left panels) and K2-24c (right panels). Top panel: ( $O - C$ ) diagram, calculated by subtracting the  $T_0$  predicted by the linear ephemeris to the observed transit times (K2, Spitzer, HST, CHEOPS). The  $O - C$  values computed from the observed  $T_0$ s are plotted with different solid colors and marker shapes, while the  $O - C$  values computed at the same epochs by the best-fit TRADES dynamical model (Section 4) are plotted as black open circles. Samples drawn from the posterior distribution from TRADES within HDI are shown as gray lines. Bottom panel: Residuals computed as the difference between observed and simulated  $T_0$ s.

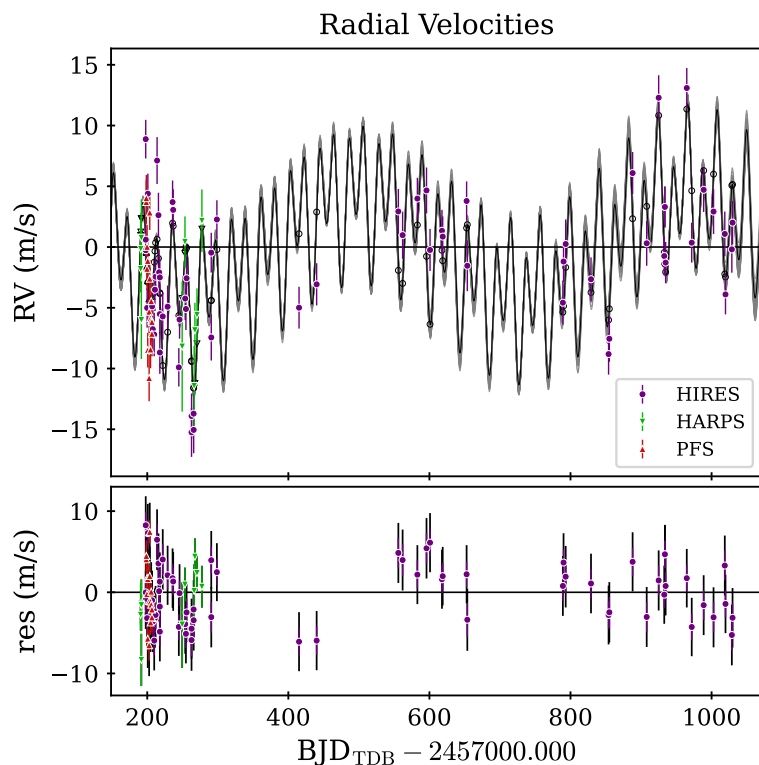


**Fig. 5.** Radial velocities of K2-24. Upper panel: RV plot; each data set (HIRES, HARPS, PFS) is plotted with a different marker shape and color, as in legend. The MAP RV model from the best-fit TRADES orbital solution is plotted as a black line, while the RV points computed at the observed epochs are rendered with open black circles. Samples drawn from the posterior distribution within HDI are shown as gray lines. Lower panel: RV residuals with respect to the TRADES RV best-fit model. The corresponding jitter determined from the best-fit model has been added in quadrature to the measured uncertainty of each data point.

ported along with the associated uncertainty in electronic form at CDS. The predicted transit times and their associated uncertainties were calculated by integrating 100 orbital solutions randomly chosen from the TRADES fit posterior and then computing the median and the 68.27% HDI interval at each transit epoch.

## 5. Discussion and conclusions

In our work, we have merged all the available space-based photometry of K2-24b and -c (including 13 unpublished CHEOPS light curves; Section 2) and derived improved stellar parameters for K2-24 (Table 1) to perform a global transit fit (Section 3), which yielded a homogeneous set of planetary parameters and

**Table 3.** Transit times of K2-24b and K2-24c measured or adopted for our dynamical analysis.

Planet	Instrument	$T_0$ [BJD <sub>TDB</sub> ]	Source
-b	K2	2456905.79529 ± 0.00035	this work
-c	K2	2456915.62477 ± 0.00021	this work
-b	K2	2456926.67909 ± 0.00049	this work
-b	K2	2456947.56565 ± 0.00035	this work
-c	K2	2456957.98825 ± 0.00019	this work
-b	K2	2456968.45070 ± 0.00033	this work
-b	Spitzer	2457323.61610 ± 0.00110	P18
-c	Spitzer	2457339.00020 ± 0.00140	P18
-c	Spitzer	2457550.50740 ± 0.00150	P18
-b	Spitzer	2457553.50490 ± 0.00160	P18
-b	HST	2457574.40950 ± 0.00350	this work
-b	CHEOPS	2459391.82076 ± 0.00064	this work, b1
-b	CHEOPS	2459412.70870 ± 0.00125	this work, b2
-c	CHEOPS	2459413.46115 ± 0.00094	this work, c1
-c	CHEOPS	2459667.64590 ± 0.00175	this work, c2
-b	CHEOPS	2459705.07047 ± 0.00082	this work, b3
-c	CHEOPS	2459710.02459 ± 0.00054	this work, c3
-b	CHEOPS	2459725.94986 ± 0.00062	this work, b4
-b	CHEOPS	2459746.83330 ± 0.00320	this work, b5
-c	CHEOPS	2459752.39985 ± 0.00093	this work, c4
-c	CHEOPS	2460049.00500 ± 0.00076	this work, c5
-c	CHEOPS	2460091.36711 ± 0.00105	this work, c6
-b	CHEOPS	2460101.84061 ± 0.00066	this work, b6
-b	CHEOPS	2460122.73033 ± 0.00066	this work, b7

**Notes.** The columns give the following: planet name (K2-24b or K2-24c), instrument used, best-fit transit time  $T_0$  in the BJD-TDB standard (Eastman et al. 2010) along with its  $1-\sigma$  error bar (symmetrized), and the source (plus the light curve ID from Table A.1 for the CHEOPS data). All the  $T_0$  values from this work were obtained through the global photometric fit described in Section 3.

transit times (Tables 2, 3). Then we fitted the latter together with all the available RVs (HIRES, PFS, HARPS) through an RV plus TTV dynamical model (Section 4) in order to get a complete orbital solution for K2-24b and -c, and for candidate planet d as well (Table 4).

### 5.1. Planetary parameters of K2-24b and K2-24c

All the derived parameters for planets -b and -c appear statistically consistent, at least within  $2\sigma$ , with those published by P18, but they mostly have smaller error bars due to the increased S/N of the combined data set, the improved stellar parameters, and the much larger baseline of the observations. This is particularly true for the planetary radii ( $R_b/R_\oplus = 5.64 \pm 0.06$ ,  $R_c/R_\oplus = 7.93 \pm 0.12$ ) and masses ( $M_b/M_\oplus = 20.6^{+1.6}_{-0.3}$ ,  $M_c/M_\oplus = 16.4^{+1.3}_{-0.2}$ ), for which we reached a relative error of 1% and 4-5%, respectively. We confirm the unusually low density of the outer planet ( $\rho_c = 0.181^{+0.017}_{-0.009}$  g cm<sup>-3</sup>), implying a very large gaseous envelope, possibly larger than 50% and hence challenging a core-accretion scenario due to the onset of runaway accretion (P18). Several alternative scenarios have been proposed to explain the existence of such “super-puff” planets (Gao & Zhang 2020), including light scattering from high-altitude photo-chemical hazes (Ohno & Tanaka 2021) or the presence of planetary rings on

specific configurations (Piro & Vissapragada 2020). These hypotheses, however, require follow-up by JWST to be tested.

A particularly interesting variable to discuss is the orbital eccentricity, due to its important consequences on the planetary migration mechanisms. We measured an extremely significant non-zero eccentricity for both planets  $e_b = 0.049^{+0.001}_{-0.002}$ ,  $e_c = 0.0282^{+0.0003}_{-0.0007}$ , confirming the findings by P18, who based on the Lithwick et al. (2012) theory predicted that  $e_b$  and  $e_c$  cannot both be zero. It is worth noting that our best-fit values are perfectly compatible with their constraints, even though our analysis is based on uninformative priors only and does not adopt any assumption on the distribution of the eccentricity in the *Kepler* population. We also mention that compared with the prediction of Antoniadou & Libert (2020), we found the eccentricity of -c to be at the very limit they set ( $e_c < 0.05$ ).

### 5.2. Dynamical stability

The K2-24 system hosts three planets (Table 4), including two Neptune-mass planets ( $M_b \approx 20.6 M_\oplus$ ,  $M_c \approx 16.4 M_\oplus$ ) in the vicinity of a 2:1 mean motion resonance ( $P_c/P_b \approx 2.029$ ). Following a suggestion from the referee, we first checked the dynamical stability of our orbital solution by computing the angular momentum deficit (AMD; Laskar 1997, 2000; Laskar & Petit 2017) of the whole posterior distribution. Then we explored the stability by evaluating the AMD-Hill criterion proposed in Eq. 26 of Petit et al. (2018). We found that the whole posterior is AMD-Hill stable. We also ran an N-body integration with the Mean Exponential Growth factor of Nearby Orbits (MEGNO; Cincotta & Simó 2000) indicator through the REBOUND package with the whfast integrator (Rein & Liu 2012; Rein & Tamayo 2015; Wisdom & Holman 1991; Rein & Tamayo 2016). We set a step size equal to 10% of the shorter period of the system and integrated for 10<sup>5</sup> years. We found that not only is the MAP solution stable (MEGNO = 2) but that 1000 samples randomly selected from the posterior are also stable with MEGNO  $\approx 2$ .

### 5.3. Discussion of whether K2-24b and K2-24c are on an MMR configuration

To get a wider view on the stability of the system and to assess whether the system is truly on a resonant configuration, we performed a dynamical analysis in a manner similar to other planetary systems (e. g., Correia et al. 2005, 2010). The system was integrated on a regular 2D mesh of initial conditions around the best fit, including planet d (Table 4). Each initial condition was integrated for 10<sup>4</sup> yr using the symplectic integrator SABAC4 (Laskar & Robutel 2001) with a step size of 10<sup>-3</sup> yr and general relativity corrections. Then, we performed a frequency analysis (Laskar 1990, 1993) of the mean longitude of the inner planet over two consecutive time intervals of 5000 yr, and we determine the main frequency,  $n$  and  $n'$ , respectively. The stability was measured by  $\Delta = |1 - n'/n|$ , which estimates the chaotic diffusion of the orbits. In Fig. 6, the results for planet -b (top panel) and planet -c (bottom panel) are reported in color: orange and red represent strongly chaotic and unstable trajectories; yellow indicates the transition between stable and unstable regimes; green corresponds to moderately chaotic trajectories but that are stable on gigayear timescales; and cyan and blue give extremely stable quasi-periodic orbits. The best-fit solution obtained from our analysis (Table 4) is marked with a white circle.

We observed that the best-fit solution from Table 4 is completely stable, even if we increase the eccentricities up to 0.4.

**Table 4.** Posterior and derived parameters of the K2-24 system from the dynamical fit with TRADES (Section 4).

Parameter [unit]	MAP (HDI $\pm 1\sigma$ )	Prior	P18
<i>Host star K2-24</i>			
$M_\star [M_\odot]$	$1.041^{+0.067}_{-0.016}$	$\mathcal{G}(1.091, 0.056)$	$1.07 \pm 0.06^*$
<i>Planet K2-24b</i>			
$M_b/M_\star$	$(59^{+2}_{-1}) \cdot 10^{-6}$	$\mathcal{U}(8.8 \cdot 10^{-8}, 2.8 \cdot 10^{-3})$	—
$M_b/M_\oplus$	$20.6^{+1.6}_{-0.3}$	(derived)	$19.0^{+2.2}_{-2.1}$
$P_b$ at $T_{\text{ref}}$ [days]	$20.88257^{+0.00005}_{-0.00007}$	$\mathcal{U}(18, 22)$	—
$\langle P_b \rangle^\S$ [days]	$20.8895961 \pm 0.0000096^\S$	(derived)	$20.88977^{+0.00034}_{-0.00035}$
$\sqrt{e_b} \cos \omega_b$	$0.221^{+0.003}_{-0.004}$	$\mathcal{U}(-\sqrt{0.5}, \sqrt{0.5})$	—
$\sqrt{e_b} \sin \omega_b$	$-0.0318^{+0.0013}_{-0.0016}$	$\mathcal{U}(-\sqrt{0.5}, \sqrt{0.5})$	—
$\lambda_b$ [deg]	$250.61^{+0.22}_{-0.13}$	$\mathcal{U}(0, 360)$	—
$\mathcal{M}_b$ [deg]	$78.8^{+0.8}_{-0.5}$	(derived)	—
$e_b$	$0.0498^{+0.0011}_{-0.0018}$	(derived)	$0.06 \pm 0.01$
$\omega_b$	$351.8^{+0.4}_{-0.5}$	(derived)	—
$\rho_b$ [cgs]	$0.632^{+0.054}_{-0.023}$	(derived)	$0.64^{+0.12}_{-0.10}$
$T_{\text{eq}}$ [K]	$732 \pm 11$	(derived)	—
TSM	$62 \pm 5$	(derived)	—
<i>Planet K2-24c</i>			
$M_c/M_\star$	$(47.3^{+1.8}_{-0.8}) \cdot 10^{-6}$	$\mathcal{U}(8.8 \cdot 10^{-8}, 2.8 \cdot 10^{-3})$	—
$M_c/M_\oplus$	$16.4^{+1.3}_{-0.2}$	(derived)	$15.4^{+1.9}_{-1.8}$
$P_c$ at $T_{\text{ref}}$ [days]	$42.3773^{+0.0005}_{-0.0004}$	$\mathcal{U}(40, 44)$	—
$\langle P_c \rangle^\S$ [days]	$42.34732 \pm 0.00018^\S$	(derived)	$42.3391 \pm 0.0012$
$\sqrt{e_c} \cos \omega_c$	$-0.1268^{+0.0058}_{-0.0012}$	$\mathcal{U}(-\sqrt{0.5}, \sqrt{0.5})$	—
$\sqrt{e_c} \sin \omega_c$	$0.110^{+0.004}_{-0.002}$	$\mathcal{U}(-\sqrt{0.5}, \sqrt{0.5})$	—
$\lambda_c$ [deg]	$182.15^{+0.03}_{-0.13}$	$\mathcal{U}(0, 360)$	—
$\mathcal{M}_c$ [deg]	$223.1^{+2.3}_{-0.6}$	(derived)	—
$e_c$	$0.0282^{+0.0003}_{-0.0007}$	(derived)	$< 0.07$ (90% conf.) $^\ddagger$
$\omega_c$	$139.0^{+0.6}_{-2.5}$	(derived)	—
$\rho_c$ [cgs]	$0.181^{+0.017}_{-0.009}$	(derived)	$0.20^{+0.04}_{-0.03}$
$T_{\text{eq}}$ [K]	$591 \pm 12$	(derived)	—
TSM	$177 \pm 16$	(derived)	—
<i>Candidate K2-24d</i>			
$M_d/M_\star$	$(155^{+19}_{-13}) \cdot 10^{-6}$	$\mathcal{U}(8.8 \cdot 10^{-8}, 2.8 \cdot 10^{-3})$	—
$M_d/M_\oplus$	$54^{+9}_{-4}$	(derived)	$52 \pm 14$
$P_d$ [days]	$469^{+10}_{-15}$	$\mathcal{U}(100, 1000)$	$440^{? \ddagger}$
$\lambda_d$ [deg]	$83^{+15}_{-12}$	$\mathcal{U}(0, 360)$	—
$\mathcal{M}_d$ [deg]	$173^{+15}_{-12}$	(derived)	—
$e_d$	0.00	(circular)	(circular)
<i>Jitter and offset terms</i>			
$\gamma_{\text{HIRES}}$ [m/s]	$1.1^{+0.4}_{-0.4}$	$\mathcal{U}(-5000, 5000)$	—
$\gamma_{\text{HARPS}}$ [m/s]	$763.1^{+0.6}_{-0.9}$	$\mathcal{U}(-5000, 5000)$	—
$\gamma_{\text{PFS}}$ [m/s]	$5.3^{+0.8}_{-1.0}$	$\mathcal{U}(-5000, 5000)$	—
$j_{\text{HIRES}}$ [m/s]	$3.2^{+0.4}_{-0.2}$	$\mathcal{U}(10^{-15}, 100)$	—
$j_{\text{HARPS}}$ [m/s]	$0.0^{+0.0}_{-0.0}$	$\mathcal{U}(10^{-15}, 100)$	—
$j_{\text{PFS}}$ [m/s]	$3.3^{+0.6}_{-0.6}$	$\mathcal{U}(10^{-15}, 100)$	—

**Notes.** All the parameters were computed at the reference time  $T_{\text{ref}} = 2456905$  BJD<sub>TDB</sub>. The columns give the parameter name, the MAP value of the posterior distribution and its 1- $\sigma$  HDI, the adopted prior, and the best-fit values from P18 for comparison (when available). \*Derived from spectroscopy; not a fitted parameter within the P18 dynamical model.  $^\S$ Average orbital period corresponding to the MAP model computed by TRADES.  $^\ddagger$ The value of  $e_c$  from P18 was derived by assuming a prior based on the distribution of  $\langle e \rangle$  observed in *Kepler* multi-planet systems.  $^\ddagger$ The best-fit period  $P_d$  and its associated uncertainty are not explicitly reported by P18.

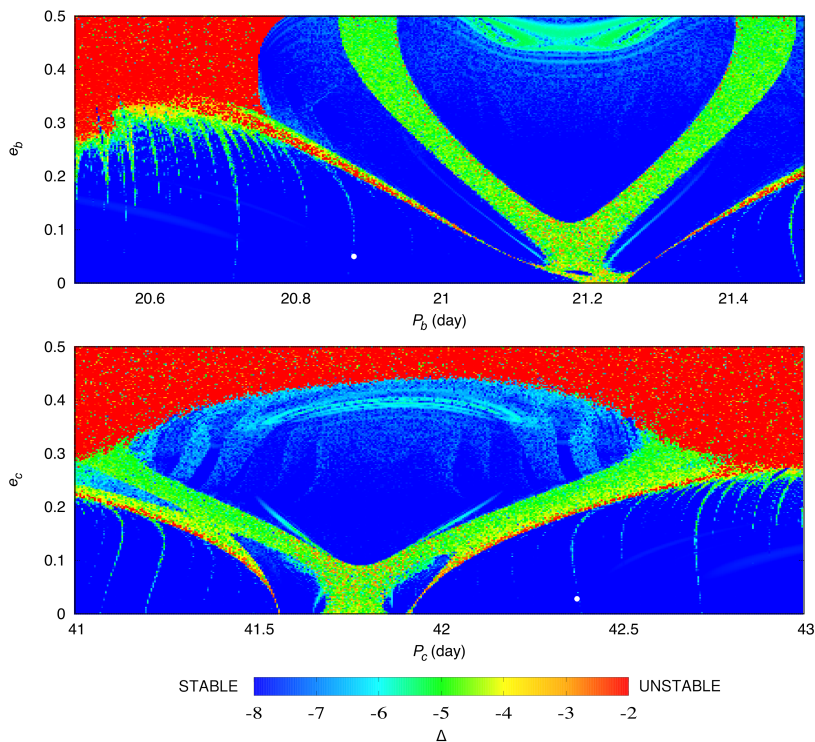


**Fig. 6.** Stability analysis of the K2-24 planetary system. For fixed initial conditions (Table 4), the parameter space of the system was explored by varying the orbital period and the eccentricity of planet -b (top panel) and of planet -c (bottom panel). The step size is 0.0025 in the eccentricities, 0.0025 d in the orbital period of planet *b*, and 0.005 d in the orbital period of planet *c*. For each initial condition, the system was integrated over  $10^4$  yr, and a stability indicator was calculated, which involved a frequency analysis of the mean longitude of the inner planet. The chaotic diffusion was measured by the variation in the frequency (see text). Red points correspond to highly unstable orbits, while blue points correspond to orbits that are likely to be stable on gigayear timescales. The white dots show the values of the best-fit solution (Table 4).

However, for eccentricities up to 0.1, which include the current best-fit determination ( $e_b \approx 0.05$ ,  $e_c \approx 0.03$ ), we observe that the system is outside the 2:1 mean motion resonance, which corresponds to the large stable structure above the V-shape chaotic region in the middle of the figures. The TTV analysis constrained the resonant part of the architecture, as can be seen in Fig. 7. In that figure, we observed that the posterior of the fit lies outside the formal resonant domain (red area), unlike, for example, TOI-216, *Kepler-1705*, or *Kepler-1972* (Nesvorný et al. 2022; Leleu et al. 2022). We conclude that the K2-24 three-planet orbital solution presented in Table 4 is not in resonance but still reliable and supple to the uncertainties in the determination of the eccentricities of the two innermost planets.

We also note that the system is on the correct side of the resonance predicted by planetary migration models (e.g., Lissauer et al. 2011). This feature is usually attributed to tidal interactions with the parent star (e.g., Delisle & Laskar 2014), but in this case this mechanism does not seem to be very efficient because the orbital period of the inner Neptune-like planet is much longer than five days (Correia et al. 2020).

Finally, with the best-fit solution, we monitored the evolution over 10 000 years of some parameters of the inner pair, including the period ratio  $P_c/P_b$ , the difference between the arguments of the pericenter  $\Delta\omega$ , and the critical resonant angles  $\phi_1$ ,  $\phi_2$  (Fig. A.4). Interestingly,  $\phi_1$  and  $\phi_2$  circulate (as one would expect from a non-MMR configuration, thus confirming our previous finding), while  $\Delta\omega$  librates in an anti-aligned ( $180^\circ$ ) configuration. Following a more quantitative approach, we repeated the same analysis on 10 000 random samples from the posterior and found that for 100% of them  $\Delta\omega$  is confined between  $\sim 140^\circ$  and  $\sim 220^\circ$  with a mean value perfectly centered on  $180^\circ$ , therefore confirming the anti-aligned scenario.

#### 5.4. Candidate planet K2-24d

It is worth noting that we independently confirmed the RV signal of the planet candidate K2-24d – previously only tentatively detected by P18 on HIRES data alone. While its parameters appear consistent, our circular fit yielded an  $8\text{-}\sigma$  detection at  $M_d/M_\oplus = 54^{+9}_{-4}$ . The period ratio with respect to the inner planets is too large (and too far from an MMR) to generate a detectable TTV on the inner planets; hence all the constraints on  $M_d$  comes from RVs. At  $P_d \approx 470$  d, the a priori transit probability (Winn 2010) of planet d would be approximately just  $R_\star/a \approx 0.4\%$ , yet the actual chances are much better than that since multiple planetary systems are very likely to be coplanar (Fabrycky et al. 2014). Unfortunately, the fraction of orbital phase currently mapped by K2, Spitzer, and CHEOPS together (all of which are capable of detecting the transit of a  $\sim 50 M_\oplus$  planet at high confidence) is only  $< 20\%$ , so no conclusion can be drawn about the orbital inclination of -d. We will continue to consider planet d as a candidate rather than a confirmed planet since we did not run any specific validation test for it, as such tests are outside the main scope of this paper.

#### 5.5. Future prospects for follow-up

The K2-24 system appears to be a very promising target for a follow-up with several current and future facilities. To this purpose, the list of predicted transit windows we tabulated (available in electronic form at CDS) is crucial to reliably schedule observations. The most obvious science case is a deeper study of its dynamical architecture, including modeling of new transit timings that could unveil additional companions on orbits on external MMRs to planet *c*.<sup>10</sup> Both planets, and -c in particular, are also compelling targets for transmission spectroscopy since

<sup>10</sup> A planet internal to -b (i.e., at  $P \lesssim 20$  d) is easily discarded by K2 photometry if it is on transiting configurations. Even if we postulate a non-transiting geometry due to an unusually high mutual inclination,

their low bulk density combined with the brightness of their host star ( $V \simeq 11.3$ ,  $J \simeq 9.6$ ,  $K \simeq 9.2$ ) offers a unique opportunity to probe the atmospheres of a pair of warm sub-Saturns close to an MMR and to link their composition with their formation site and migration history (Libby-Roberts et al. 2020). If we compute the transmission spectroscopy metric (TSM; Kempton et al. 2018) based on our newly derived parameters on Tables 1, 2 and 4, we get  $62 \pm 5$  for -b and  $177 \pm 16$  for -c (TSM-scaled factor computer for  $> 4 R_{\oplus}$  planets). We highlight that a value of 90 is usually considered the threshold to select the best targets amenable to atmospheric characterization with JWST (Kempton et al. 2018). As already mentioned (Section 2.2), HST, through WFC3/NIR, has already been exploited to search for atmospheric features on K2-24b, unfortunately with a null result. Edwards et al. (2023b) noted, however, that the best-fit free chemistry model was preferred to a flat line at  $2.5\sigma$ , suggesting the presence of  $\text{NH}_3$ , but without evidence for  $\text{H}_2\text{O}$ .

For the first time, TESS will observe K2-24 in Sector 91 of Cycle 7, currently planned from 2025 April 9 to May 7. According to our modeling, only one event will be captured: a transit of K2-24b at 2025-04-25T21:15:40 UTC, unfortunately close to the mid-sector gap. It is difficult at this stage to predict whether or not TESS will manage to add new data to the TTV analysis. The availability of a new, well-constrained ephemeris, on the other hand, opens an interesting opportunity for a ground-based follow-up campaign from the southern hemisphere. Both transit depths (approx. 2000 and 4000 ppm, respectively) are feasible, with most medium-sized telescopes operating with the defocusing technique (Nascimbeni et al. 2011), and even partial transits would provide reliable transit times and help in mapping the TTV signal, as the transit shape parameters of both planets (including duration) are now constrained at high precision (Table 2).

As a closing note, we mention that in the next years both PLATO (Rauer et al. 2014) and Ariel (Tinetti et al. 2021) could provide follow-up of K2-24. PLATO, to be launched in 2026, will unfortunately not observe this target during its long-pointing operation phase since K2-24 lies too close to the ecliptic to meet the engineering constraints. However, it could be monitored at a later stage for a shorter duration (two to three months) during the so-called short-duration observing phase (Nascimbeni et al. 2022). Ariel, on the other hand, will observe transits of K2-24b and -c in Tier 1 and 3, respectively (Edwards & Tinetti 2022). A detailed study (Borsato et al. 2022) demonstrated that the Ariel FGS light curves of K2-24 can also be exploited for accurate TTV analysis and that ten transits would be enough to constrain the presence of an external resonant companion down to the rocky regime.

**Acknowledgements.** We thank the anonymous referee for her/his valuable comments and suggestions. CHEOPS is an ESA mission in partnership with Switzerland with important contributions to the payload and the ground segment from Austria, Belgium, France, Germany, Hungary, Italy, Portugal, Spain, Sweden, and the United Kingdom. The CHEOPS Consortium would like to gratefully acknowledge the support received by all the agencies, offices, universities, and industries involved. Their flexibility and willingness to explore new approaches were essential to the success of this mission. CHEOPS data analyzed in this article will be made available in the CHEOPS mission archive ([https://cheops.unige.ch/archive\\_browser/](https://cheops.unige.ch/archive_browser/)). VNa, LBo, TZi, GPI, GMa, IPa, RRa, and GSc acknowledge support from CHEOPS ASI-INAF agreement n. 2019-29-HH.0. S.G.S. acknowledge support from FCT through FCT contract nr. CEECIND/00826/2018 and POPH/FSE (EC). The Portuguese team thanks the Portuguese Space Agency for the provision of financial support in the framework of the PRODEX Programme of the European Space Agency (ESA) under contract number 4000142255. TWi acknowledges support from the UKSA and

the currently available RVs would put an upper limit to its mass in the rocky planet regime.

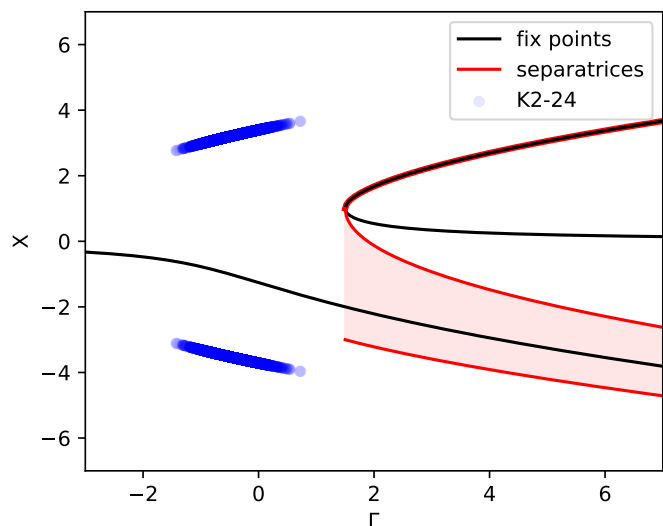


**Fig. 7.** One-degree of freedom model of the 2:1 MMR (Henrard & Lemaître 1983; Deck et al. 2013). We note that  $X$  and  $\Gamma$  are functions of the orbital elements and the masses of the system. The term  $\Gamma$  represents how deep the system is in the resonance, while  $X$  parameterizes the position of the fix points and separatrices. The blue dots represent the intersection of 10 000 randomly selected samples of the posterior with the  $X$ - $\Gamma$  plane.

the University of Warwick. YAl acknowledges support from the Swiss National Science Foundation (SNSF) under grant 200020\_192038. We acknowledge financial support from the Agencia Estatal de Investigación of the Ministerio de Ciencia e Innovación MCIN/AEI/10.13039/501100011033 and the ERDF “A way of making Europe” through projects PID2019-107061GB-C61, PID2019-107061GB-C66, PID2021-125627OB-C31, and PID2021-125627OB-C32, from the Centre of Excellence “Severo Ochoa” award to the Instituto de Astrofísica de Canarias (CEX2019-000920-S), from the Centre of Excellence “María de Maeztu” award to the Institut de Ciències de l’Espai (CEX2020-001058-M), and from the Generalitat de Catalunya/CERCA programme. DBa, EPa, and IRI acknowledge financial support from the Agencia Estatal de Investigación of the Ministerio de Ciencia e Innovación MCIN/AEI/10.13039/501100011033 and the ERDF “A way of making Europe” through projects PID2019-107061GB-C61, PID2019-107061GB-C66, PID2021-125627OB-C31, and PID2021-125627OB-C32, from the Centre of Excellence “Severo Ochoa” award to the Instituto de Astrofísica de Canarias (CEX2019-000920-S), from the Centre of Excellence “María de Maeztu” award to the Institut de Ciències de l’Espai (CEX2020-001058-M), and from the Generalitat de Catalunya/CERCA programme. A.C.M.C. acknowledges support from the FCT, Portugal, through the CFisUC projects UIDB/04564/2020 and UIDP/04564/2020, with DOI identifiers 10.54499/UIDB/04564/2020 and 10.54499/UIDP/04564/2020, respectively. S.C.B. acknowledges support from FCT through FCT contracts nr. IF/01312/2014/CP1215/CT0004. 0000-0003-0312-313X. A.C., A.D., B.E., K.G., and J.K. acknowledge their role as ESA-appointed CHEOPS Science Team Members. ABr was supported by the SNSA. CBr and ASi acknowledge support from the Swiss Space Office through the ESA PRODEX program. ACC acknowledges support from STFC consolidated grant number ST/V000861/1, and UKSA grant number ST/X002217/1. P.E.C. is funded by the Austrian Science Fund (FWF) Erwin Schrodinger Fellowship, program J4595-N. This project was supported by the CNES. The Belgian participation to CHEOPS has been supported by the Belgian Federal Science Policy Office (BELSPO) in the framework of the PRODEX Program, and by the University of Liège through an ARC grant for Concerted Research Actions financed by the Wallonia-Brussels Federation. L.D. thanks the Belgian Federal Science Policy Office (BELSPO) for the provision of financial support in the framework of the PRODEX Programme of the European Space Agency (ESA) under contract number 4000142531. This work was supported by FCT - Fundação para a Ciência e a Tecnologia through national funds and by FEDER through COMPETE2020 through the research grants UIDB/04434/2020, UIDP/04434/2020, 2022.06962.PTDC. O.D.S.D. is supported in the form of work contract (DL 57/2016/CP1364/CT0004) funded by national funds through FCT. B.-O. D. acknowledges support from the Swiss State Secretariat for Education, Research and Innovation (SERI) under contract number MB22.00046. This project has received funding from the Swiss National Science Foundation for project 200021\_200726. It has also been carried out within the framework of the National Centre of Competence in Research PlanetS sup-

ported by the Swiss National Science Foundation under grant 51NF40\_205606. The authors acknowledge the financial support of the SNSF. MF and CMP gratefully acknowledge the support of the Swedish National Space Agency (DNR 65/19, 174/18). DG gratefully acknowledges financial support from the CRT foundation under Grant No. 2018.2323 “Gaseous or rocky? Unveiling the nature of small worlds”. M.G. is an F.R.S.-FNRS Senior Research Associate. MNG is the ESA CHEOPS Project Scientist and Mission Representative, and as such also responsible for the Guest Observers (GO) Programme. MNG does not relay proprietary information between the GO and Guaranteed Time Observation (GTO) Programmes, and does not decide on the definition and target selection of the GTO Programme. CHE acknowledges support from the European Union H2020-MSCA-ITN-2019 under Grant Agreement no. 860470 (CHAMELEON). KGI is the ESA CHEOPS Project Scientist and is responsible for the ESA CHEOPS Guest Observers Programme. She does not participate in, or contribute to, the definition of the Guaranteed Time Programme of the CHEOPS mission through which observations described in this paper have been taken, nor to any aspect of target selection for the programme. K.W.F.L. was supported by Deutsche Forschungsgemeinschaft grants RA714/14-1 within the DFG Schwerpunkt SPP 1992, Exploring the Diversity of Extrasolar Planets. This work was granted access to the HPC resources of MesoPSL financed by the Region Ile de France and the project Equip@Meso (reference ANR-10-EQPX-29-01) of the programme Investissements d’Avenir supervised by the Agence Nationale pour la Recherche. ML acknowledges support of the Swiss National Science Foundation under grant number PCEFP2\_194576. PM acknowledges support from STFC research grant number ST/R000638/1. This work was also partially supported by a grant from the Simons Foundation (PI Queloz, grant number 327127). NCSa acknowledges funding by the European Union (ERC, FIERCE, 101052347). Views and opinions expressed are however those of the author(s) only and do not necessarily reflect those of the European Union or the European Research Council. Neither the European Union nor the granting authority can be held responsible for them. GyMSz acknowledges the support of the Hungarian National Research, Development and Innovation Office (NKFIH) grant K-125015, a PRODEX Experiment Agreement No. 4000137122, the Lendület LP2018-7/2021 grant of the Hungarian Academy of Science and the support of the city of Szombathely. V.V.G. is an F.R.S.-FNRS Research Associate. JV acknowledges support from the Swiss National Science Foundation (SNSF) under grant PZ00P2\_208945. NAW acknowledges UKSA grant ST/R004838/1. Ple acknowledges that this publication was produced while attending the PhD program in Space Science and Technology at the University of Trento, Cycle XXXVIII, with the support of a scholarship co-financed by the Ministerial Decree no. 351 of 9th April 2022, based on the NRRP - funded by the European Union - NextGenerationEU - Mission 4 “Education and Research”, Component 2 “From Research to Business”, Investment 3.3 – CUP E63C22001340001. E.V. acknowledges support from the ‘DIS-COBOLO’ project funded by the Spanish Ministerio de Ciencia, Innovación y Universidades under grant PID2021-127289NB-I00. This work has been carried out within the framework of the NCCR PlanetS supported by the Swiss National Science Foundation under grants 51NF40\_182901 and 51NF40\_205606. AL acknowledges support of the Swiss National Science Foundation under grant number TMSGI2\_211697.

## References

Agol, E. & Fabrycky, D. C. 2018, in *Handbook of Exoplanets*, ed. H. J. Deeg & J. A. Belmonte (Springer International Publishing), 7

Agol, E., Steffen, J., Sari, R., & Clarkson, W. 2005, *MNRAS*, 359, 567

Akeson, R. L., Chen, X., Ciardi, D., et al. 2013, *PASP*, 125, 989

Antoniadou, K. I. & Libert, A.-S. 2020, *A&A*, 640, A55

Auvergne, M., Bodin, P., Boissard, L., et al. 2009, *A&A*, 506, 411

Barros, S. C. C., Boué, G., Gibson, N. P., et al. 2013, *MNRAS*, 430, 3032

Batygin, K. 2015, *MNRAS*, 451, 2589

Benneke, B., Werner, M., Petigura, E., et al. 2017, *ApJ*, 834, 187

Benz, W., Broeg, C., Fortier, A., et al. 2021, *Experimental Astronomy*, 51, 109

Borsato, L., Malavolta, L., Piotto, G., et al. 2019, *MNRAS*, 484, 3233

Borsato, L., Marzari, F., Nascimbeni, V., et al. 2014, *A&A*, 571, A38

Borsato, L., Nascimbeni, V., Piotto, G., & Szabó, G. 2022, *Experimental Astronomy*, 53, 635

Borsato, L., Piotto, G., Gandolfi, D., et al. 2021, *MNRAS*, 506, 3810

Borucki, W. J., Koch, D., Basri, G., et al. 2010, *Science*, 327, 977

Bozhilov, V., Antonova, D., Hobson, M. J., et al. 2023, *ApJ*, 946, L36

Cincotta, P. M. & Simó, C. 2000, *A&AS*, 147, 205

Correia, A. C. M., Bourrier, V., & Delisle, J. B. 2020, *A&A*, 635, A37

Correia, A. C. M., Couetdic, J., Laskar, J., et al. 2010, *A&A*, 511, A21

Correia, A. C. M., Udry, S., Mayor, M., et al. 2005, *A&A*, 440, 751

Dai, F., Winn, J. N., Albrecht, S., et al. 2016, *ApJ*, 823, 115

Deck, K. M., Payne, M., & Holman, M. J. 2013, *ApJ*, 774, 129

Delisle, J. B. & Laskar, J. 2014, *A&A*, 570, L7

Deming, D., Knutson, H., Kammer, J., et al. 2015, *ApJ*, 805, 132

Eastman, J., Siverd, R., & Gaudi, B. S. 2010, *PASP*, 122, 935

Edwards, B., Changeat, Q., Tsiaras, A., et al. 2023a, *AJ*, 166, 158

Edwards, B., Changeat, Q., Tsiaras, A., et al. 2023b, *ApJS*, 269, 31

Edwards, B. & Tinetti, G. 2022, *AJ*, 164, 15

Fabrycky, D. C., Lissauer, J. J., Ragozzine, D., et al. 2014, *ApJ*, 790, 146

Foreman-Mackey, D., Hogg, D. W., Lang, D., & Goodman, J. 2013, *PASP*, 125, 306

Fortier, A., Simon, A. E., Broeg, C., et al. 2024, *A&A*, 687, A302

Gaia Collaboration, Vallenari, A., Brown, A. G. A., et al. 2023, *A&A*, 674, A1

Gao, P. & Zhang, X. 2020, *ApJ*, 890, 93

Gelman, A. & Rubin, D. B. 1992, *Statistical Science*, 7, 457

Geweke, J. F. 1991, Evaluating the accuracy of sampling-based approaches to the calculation of posterior moments, Staff Report 148, Federal Reserve Bank of Minneapolis

Hadden, S. & Lithwick, Y. 2016, *ApJ*, 828, 44

Hamann, A., Montet, B. T., Fabrycky, D. C., Agol, E., & Kruse, E. 2019, *AJ*, 158, 133

Henrard, J. & Lemaître, A. 1983, *Celestial Mechanics*, 30, 197

Holman, M. J., Fabrycky, D. C., Ragozzine, D., et al. 2010, *Science*, 330, 51

Holman, M. J. & Murray, N. W. 2005, *Science*, 307, 1288

Howell, S. B., Sobek, C., Haas, M., et al. 2014, *PASP*, 126, 398

Hoyer, S., Guterman, P., Demangeon, O., et al. 2020, *A&A*, 635, A24

Huang, S. & Ormel, C. W. 2023, *MNRAS*, 522, 828

Kempton, E. M. R., Bean, J. L., Louie, D. R., et al. 2018, *PASP*, 130, 114401

Kipping, D. M. 2013, *MNRAS*, 435, 2152

Kreidberg, L. 2015, *PASP*, 127, 1161

Laskar, J. 1990, *Icarus*, 88, 266

Laskar, J. 1993, *Physica D Nonlinear Phenomena*, 67, 257

Laskar, J. 1997, *A&A*, 317, L75

Laskar, J. 2000, *Phys. Rev. Lett.*, 84, 3240

Laskar, J. & Petit, A. C. 2017, *A&A*, 605, A72

Laskar, J. & Robutel, P. 2001, *Celestial Mechanics and Dynamical Astronomy*, 80, 39

Leleu, A., Delisle, J. B., Mardling, R., et al. 2022, *A&A*, 661, A141

Libby-Roberts, J. E., Berta-Thompson, Z. K., Désert, J.-M., et al. 2020, *AJ*, 159, 57

Lissauer, J. J., Ragozzine, D., Fabrycky, D. C., et al. 2011, *ApJS*, 197, 8

Lithwick, Y. & Wu, Y. 2012, *ApJ*, 756, L11

Lithwick, Y., Xie, J., & Wu, Y. 2012, *ApJ*, 761, 122

Malavolta, L., Borsato, L., Granata, V., et al. 2017, *AJ*, 153, 224

Malavolta, L., Mayo, A. W., Loudon, T., et al. 2018, *AJ*, 155, 107

Malavolta, L., Nascimbeni, V., Piotto, G., et al. 2016, *A&A*, 588, A118

Mills, S. M., Fabrycky, D. C., Migaszewski, C., et al. 2016, *Nature*, 533, 509

Nascimbeni, V., Borsato, L., Zingales, T., et al. 2023, *A&A*, 673, A42

Nascimbeni, V., Piotto, G., Bedin, L. R., & Damasso, M. 2011, *A&A*, 527, A85

Nascimbeni, V., Piotto, G., Börner, A., et al. 2022, *A&A*, 658, A31

Nelson, B., Ford, E. B., & Payne, M. J. 2014, *ApJS*, 210, 11

Nesvorný, D., Chrenko, O., & Flock, M. 2022, *ApJ*, 925, 38

Ohno, K. & Tanaka, Y. A. 2021, *ApJ*, 920, 124

Parviainen, H. & Aigrain, S. 2015, *MNRAS*, 453, 3821

Parviainen, H., Pallé, E., Nortmann, L., et al. 2016, *A&A*, 585, A114

Petigura, E. A., Benneke, B., Batygin, K., et al. 2018, *AJ*, 156, 89

Petigura, E. A., Howard, A. W., Lopez, E. D., et al. 2016, *ApJ*, 818, 36

Petigura, E. A., Livingston, J., Batygin, K., et al. 2020, *AJ*, 159, 2

Petit, A. C., Laskar, J., & Boué, G. 2018, *A&A*, 617, A93

Piro, A. L. & Vissapragada, S. 2020, *AJ*, 159, 131

Rauer, H., Catala, C., Aerts, C., et al. 2014, *Experimental Astronomy*, 38, 249

Rein, H. & Liu, S. F. 2012, *A&A*, 537, A128

Rein, H. & Tamayo, D. 2015, *MNRAS*, 452, 376

Rein, H. & Tamayo, D. 2016, *MNRAS*, 459, 2275

Ricker, G. R., Winn, J. N., Vanderspek, R., et al. 2015, *Journal of Astronomical Telescopes, Instruments, and Systems*, 1, 014003

Sanchis-Ojeda, R., Fabrycky, D. C., Winn, J. N., et al. 2012, *Nature*, 487, 449

ter Braak, C. J. F. & Vrugt, J. A. 2008, *Statistics and Computing*, 18, 435

Teysandier, J. & Libert, A.-S. 2020, *A&A*, 643, A11

Tinetti, G., Drossart, P., Eccleston, P., et al. 2018, *Experimental Astronomy*, 46, 135

Tinetti, G., Eccleston, P., Haswell, C., et al. 2021, *arXiv e-prints*, arXiv:2104.04824

Trifonov, T., Brahm, R., Jordán, A., et al. 2023, *AJ*, 165, 179

Tsiaras, A., Rocchetto, M., Waldmann, I. P., et al. 2016a, *ApJ*, 820, 99

Tsiaras, A., Waldmann, I. P., Rocchetto, M., et al. 2016b, *ApJ*, 832, 202

Tsiaras, A., Waldmann, I. P., Zingales, T., et al. 2018, *AJ*, 155, 156

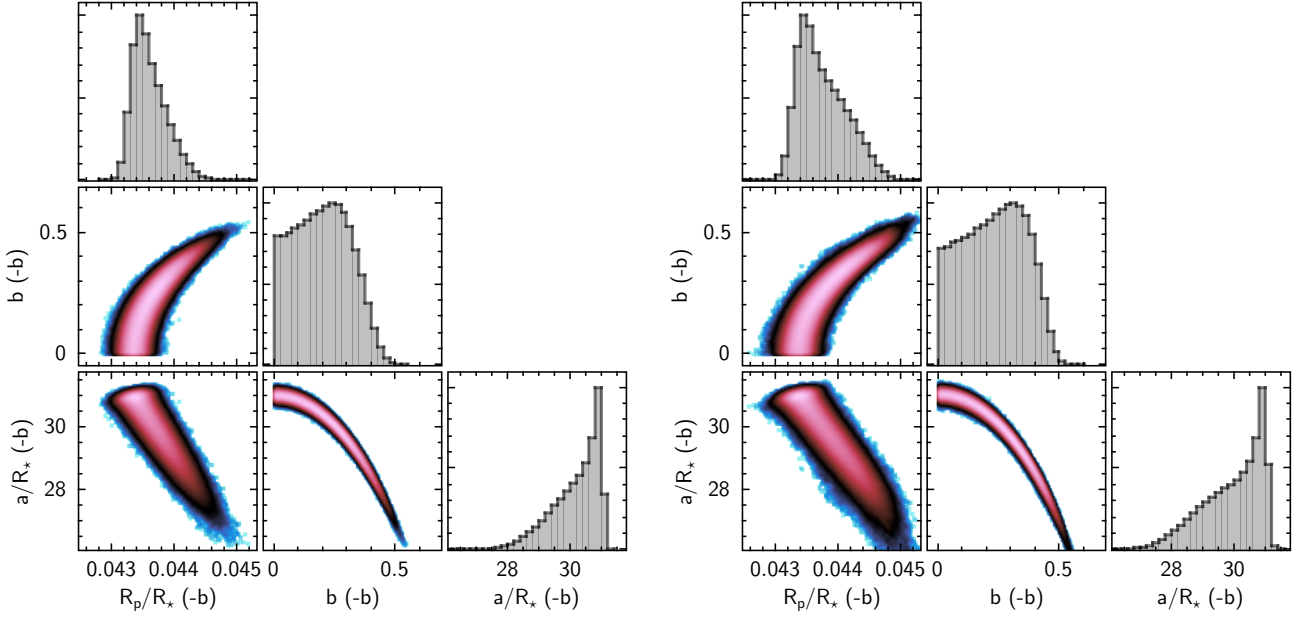
Vanderburg, A. & Johnson, J. A. 2014, *PASP*, 126, 948

Weiss, L. M., Fabrycky, D. C., Agol, E., et al. 2020, *AJ*, 159, 242

Winn, J. N. 2010, in *Exoplanets*, ed. S. Seager, 55–77

Wisdom, J. & Holman, M. 1991, *AJ*, 102, 1528

- <sup>1</sup> INAF, Osservatorio Astronomico di Padova, Vicolo dell'Osservatorio 5, 35122 Padova, Italy
- <sup>2</sup> Dipartimento di Fisica e Astronomia, Università degli Studi di Padova, Vicolo dell'Osservatorio 3, 35122 Padova, Italy
- <sup>3</sup> Instituto de Astrofísica e Ciências do Espaço, Universidade do Porto, CAUP, Rua das Estrelas, 4150-762 Porto, Portugal
- <sup>4</sup> Department of Physics, University of Warwick, Gibbet Hill Road, Coventry CV4 7AL, United Kingdom
- <sup>5</sup> Weltraumforschung und Planetologie, Physikalisches Institut, University of Bern, Gesellschaftsstrasse 6, 3012 Bern, Switzerland
- <sup>6</sup> Center for Space and Habitability, University of Bern, Gesellschaftsstrasse 6, 3012 Bern, Switzerland
- <sup>7</sup> Observatoire astronomique de l'Université de Genève, Chemin Pegasi 51, 1290 Versoix, Switzerland
- <sup>8</sup> Department of Astronomy & Astrophysics, University of Chicago, Chicago, IL 60637, USA
- <sup>9</sup> Dipartimento di Fisica e Astronomia "Galileo Galilei", Università degli Studi di Padova, Vicolo dell'Osservatorio 3, 35122 Padova, Italy
- <sup>10</sup> Instituto de Astrofísica de Canarias, Vía Láctea s/n, 38200 La Laguna, Tenerife, Spain
- <sup>11</sup> Departamento de Astrofísica, Universidad de La Laguna, Astrofísico Francisco Sanchez s/n, 38206 La Laguna, Tenerife, Spain
- <sup>12</sup> Admatis, 5. Kandó Kálmán Street, 3534 Miskolc, Hungary
- <sup>13</sup> Depto. de Astrofísica, Centro de Astrobiología (CSIC-INTA), ESAC campus, 28692 Villanueva de la Cañada (Madrid), Spain
- <sup>14</sup> Departamento de Física e Astronomia, Faculdade de Ciências, Universidade do Porto, Rua do Campo Alegre, 4169-007 Porto, Portugal
- <sup>15</sup> Space Research Institute, Austrian Academy of Sciences, Schmiedlstrasse 6, A-8042 Graz, Austria
- <sup>16</sup> Max Planck Institute for Extraterrestrial Physics, Gießenbachstraße, 85748 Garching, Germany
- <sup>17</sup> Department of Astronomy, Stockholm University, AlbaNova University Center, 10691 Stockholm, Sweden
- <sup>18</sup> Physikalisches Institut, University of Bern, Gesellschaftsstrasse 6, 3012 Bern, Switzerland
- <sup>19</sup> Centre for Exoplanet Science, SUPA School of Physics and Astronomy, University of St Andrews, North Haugh, St Andrews KY16 9SS, UK
- <sup>20</sup> CFisUC, Departamento de Física, Universidade de Coimbra, 3004-516 Coimbra, Portugal
- <sup>21</sup> Institute of Planetary Research, German Aerospace Center (DLR), Rutherfordstrasse 2, 12489 Berlin, Germany
- <sup>22</sup> INAF, Osservatorio Astrofisico di Torino, Via Osservatorio, 20, I-10025 Pino Torinese To, Italy
- <sup>23</sup> Centre for Mathematical Sciences, Lund University, Box 118, 221 00 Lund, Sweden
- <sup>24</sup> Aix Marseille Univ, CNRS, CNES, LAM, 38 rue Frédéric Joliot-Curie, 13388 Marseille, France
- <sup>25</sup> Astrobiology Research Unit, Université de Liège, Allée du 6 Août 19C, B-4000 Liège, Belgium
- <sup>26</sup> Space sciences, Technologies and Astrophysics Research (STAR) Institute, Université de Liège, Allée du 6 Août 19C, 4000 Liège, Belgium
- <sup>27</sup> Institute of Astronomy, KU Leuven, Celestijnenlaan 200D, 3001 Leuven, Belgium
- <sup>28</sup> ELTE Gothard Astrophysical Observatory, 9700 Szombathely, Szent Imre h. u. 112, Hungary
- <sup>29</sup> SRON Netherlands Institute for Space Research, Niels Bohrweg 4, 2333 CA Leiden, Netherlands
- <sup>30</sup> Centre Vie dans l'Univers, Faculté des sciences, Université de Genève, Quai Ernest-Ansermet 30, 1211 Genève 4, Switzerland
- <sup>31</sup> Leiden Observatory, University of Leiden, PO Box 9513, 2300 RA Leiden, The Netherlands
- <sup>32</sup> Department of Space, Earth and Environment, Chalmers University of Technology, Onsala Space Observatory, 439 92 Onsala, Sweden
- <sup>33</sup> Dipartimento di Fisica, Università degli Studi di Torino, via Pietro Giuria 1, I-10125, Torino, Italy
- <sup>34</sup> National and Kapodistrian University of Athens, Department of Physics, University Campus, Zografos GR-157 84, Athens, Greece
- <sup>35</sup> Department of Astrophysics, University of Vienna, Türkenschanzstrasse 17, 1180 Vienna, Austria
- <sup>36</sup> European Space Agency (ESA), European Space Research and Technology Centre (ESTEC), Keplerlaan 1, 2201 AZ Noordwijk, The Netherlands
- <sup>37</sup> Institute for Theoretical Physics and Computational Physics, Graz University of Technology, Petersgasse 16, 8010 Graz, Austria
- <sup>38</sup> Konkoly Observatory, Research Centre for Astronomy and Earth Sciences, 1121 Budapest, Konkoly Thege Miklós út 15-17, Hungary
- <sup>39</sup> ELTE Eötvös Loránd University, Institute of Physics, Pázmány Péter sétány 1/A, 1117 Budapest, Hungary
- <sup>40</sup> Lund Observatory, Division of Astrophysics, Department of Physics, Lund University, Box 118, 22100 Lund, Sweden
- <sup>41</sup> IMCCE, UMR8028 CNRS, Observatoire de Paris, PSL Univ., Sorbonne Univ., 77 av. Denfert-Rochereau, 75014 Paris, France
- <sup>42</sup> Institut d'astrophysique de Paris, UMR7095 CNRS, Université Pierre & Marie Curie, 98bis blvd. Arago, 75014 Paris, France
- <sup>43</sup> Astrophysics Group, Lennard Jones Building, Keele University, Staffordshire, ST5 5BG, United Kingdom
- <sup>44</sup> European Space Agency, ESA - European Space Astronomy Centre, Camino Bajo del Castillo s/n, 28692 Villanueva de la Cañada, Madrid, Spain
- <sup>45</sup> INAF, Osservatorio Astrofisico di Catania, Via S. Sofia 78, 95123 Catania, Italy
- <sup>46</sup> Institute of Optical Sensor Systems, German Aerospace Center (DLR), Rutherfordstrasse 2, 12489 Berlin, Germany
- <sup>47</sup> ETH Zurich, Department of Physics, Wolfgang-Pauli-Strasse 2, CH-8093 Zurich, Switzerland
- <sup>48</sup> Cavendish Laboratory, JJ Thomson Avenue, Cambridge CB3 0HE, UK
- <sup>49</sup> Institut fuer Geologische Wissenschaften, Freie Universitaet Berlin, Malteserstrasse 74-100, 12249 Berlin, Germany
- <sup>50</sup> Institut de Ciències de l'Espai (ICE, CSIC), Campus UAB, Can Magrans s/n, 08193 Bellaterra, Spain
- <sup>51</sup> Institut d'Estudis Espacials de Catalunya (IEEC), 08860 Castelldefels (Barcelona), Spain
- <sup>52</sup> ESOC, European Space Agency, Robert-Bosch-Str. 5, 64293 Darmstadt, Germany
- <sup>53</sup> HUN-REN-ELTE Exoplanet Research Group, Szent Imre h. u. 112., Szombathely, H-9700, Hungary
- <sup>54</sup> Institute of Astronomy, University of Cambridge, Madingley Road, Cambridge, CB3 0HA, United Kingdom
- <sup>55</sup> Dipartimento di Fisica, Università di Trento, Via Sommarive 14, 38123 Povo (TN), Italy

**Appendix A: Additional plots and tables**


**Fig. A.1.** Corner plot of the final MCMC distribution for the transit parameters of planet K2-24b (radius ratio  $R_p/R_*$ , impact parameter  $b$ , scaled semi-major axis  $a/R_*$ ) of our LD-prior (left panel) and LD-fit (right panel) photometric modeling described in Section 3. The best-fit values are tabulated in Table 2, second and fourth column, respectively.

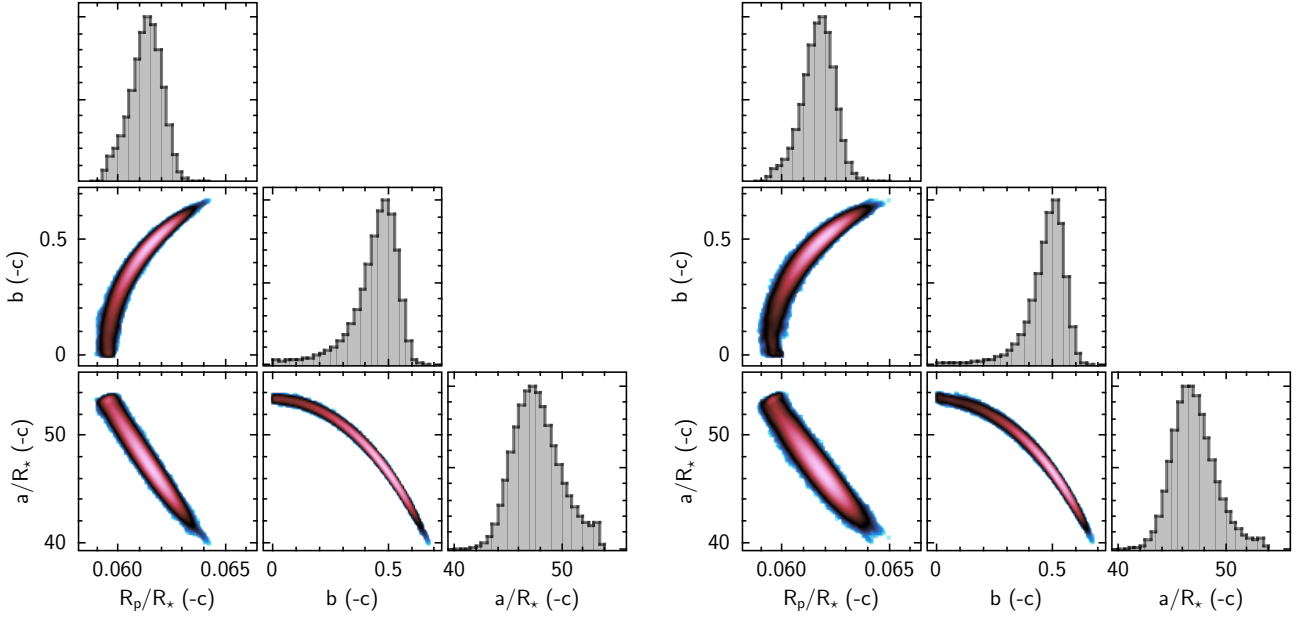


**Fig. A.2.** Corner plot of the final MCMC distribution for the transit parameters of planet K2-24c (radius ratio  $R_p/R_*$ , impact parameter  $b$ , scaled semi-major axis  $a/R_*$ ) of our LD-prior (left panel) and LD-fit (right panel) photometric modeling described in Section 3. The best-fit values are tabulated in Table 2, second and fourth column, respectively.

**Table A.1.** Log of the CHEOPS observations.

planet	ID	UT date	$N$	$\sigma$ [ppm]	key
K2-24b	b1	2021-06-26	392	606	CH_PR100025_TG006001_V0300
K2-24b	b2	2021-07-16	359	642	CH_PR100025_TG006002_V0300
K2-24c	c1	2021-07-17	433	590	CH_PR100025_TG006101_V0300
K2-24c	c2	2022-03-28	480	685	CH_PR100025_TG007101_V0300
K2-24b	b3	2022-05-05	427	732	CH_PR100025_TG007001_V0300
K2-24c	c3	2022-05-10	563	735	CH_PR100025_TG007102_V0300
K2-24b	b4	2022-05-26	433	671	CH_PR100025_TG007002_V0300
K2-24b	b5	2022-06-16	368	769	CH_PR100025_TG007003_V0300
K2-24c	c4	2022-06-21	468	728	CH_PR100025_TG007103_V0300
K2-24c	c5	2023-04-13	496	677	CH_PR100025_TG007401_V0300
K2-24c	c6	2023-05-26	504	647	CH_PR100025_TG007901_V0300
K2-24b	b6	2023-06-06	576	672	CH_PR100025_TG008001_V0300
K2-24b	b7	2023-06-27	490	618	CH_PR100025_TG008101_V0300

**Notes.** The columns give: the planet name (K2-24b or -c), the ID matching the labels in Fig. 2, the UT date at start, the number of photometric points  $N$ , the root mean square  $\sigma$  with respect to the best-fit model in parts per million, and the CHEOPS key ID.

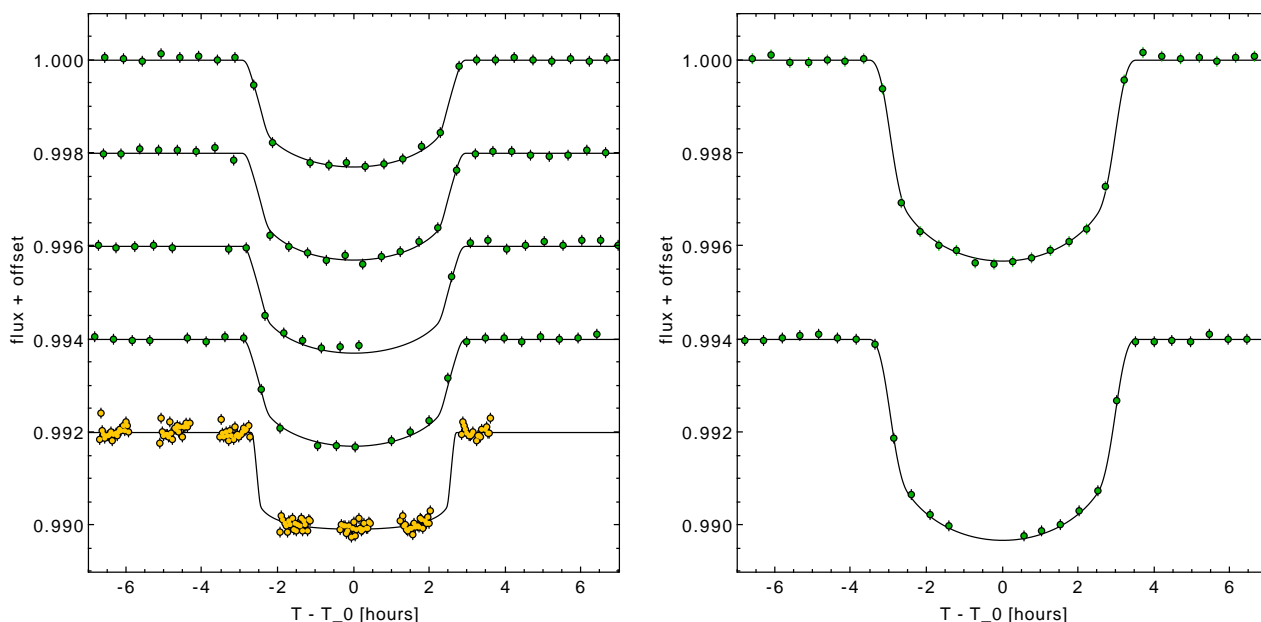


**Fig. A.3.** Light curves of K2-24b (left panel) and K2-24c (right panel) from K2 (green circles) and HST/WFC3 (yellow circles) analyzed for the present work (Section 2.1 and 2.2). The light curves are sorted in chronological order from top to bottom, as in Table 3. An arbitrary vertical offset was added for visualization.

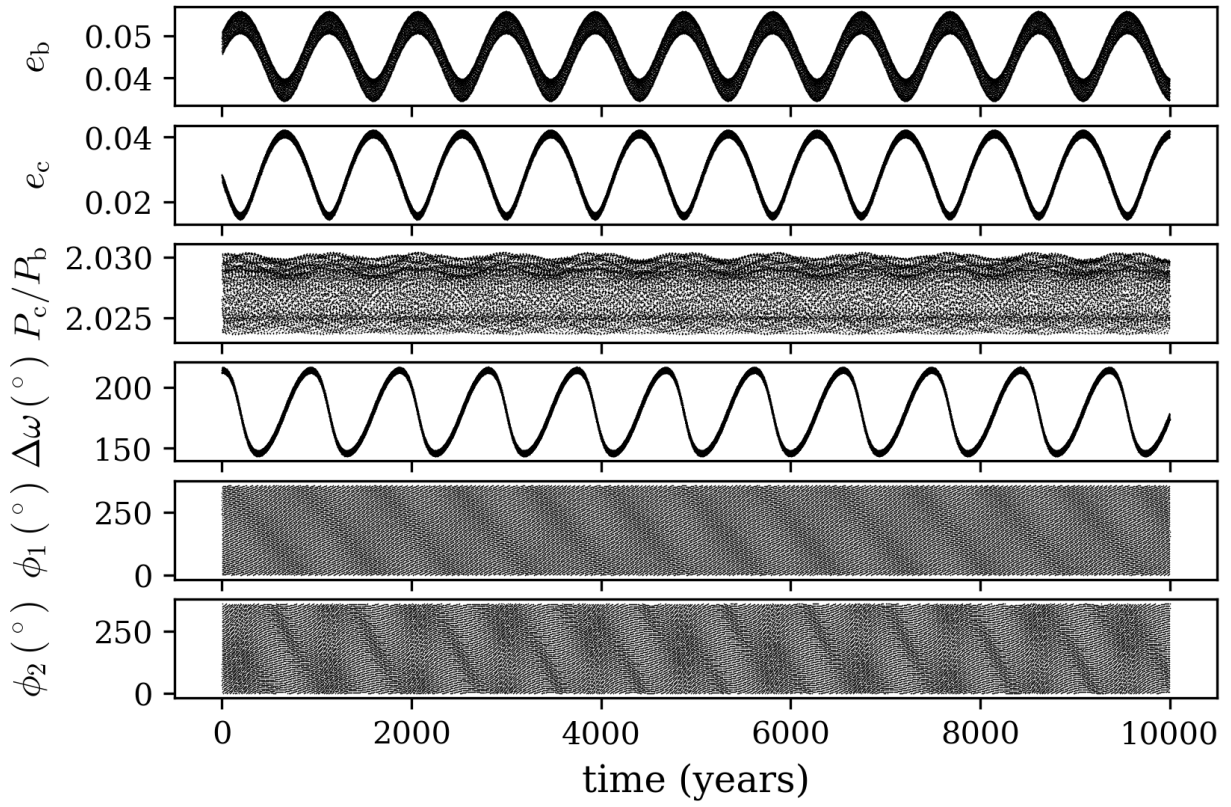


**Fig. A.4.** Evolution of the orbital parameters of K2-24b and -c, integrated over 10000 years (see Section 5.3 for details). From top to bottom: eccentricities  $e_b$ ,  $e_c$  of planet -b and -c (respectively), orbital period ratio  $P_c/P_b$ , difference between the pericenter argument  $\Delta\omega$ , critical resonant angles  $\phi_1$  and  $\phi_2$ .

**Table A.2.** Transit times of K2-24b and K2-24c predicted by our dynamic model for 2024-2025.

Planet	$T_0$ [JD]	$T_0$ [BJD <sub>TDB</sub> ]	$\sigma(T_0)$ [d]	$T_0$ [UTC]
-b	2460310.7396	2460310.7434	0.0013	2024-01-01T05:50:34
-b	2460331.6350	2460331.6373	0.0016	2024-01-22T03:17:47
-c	2460345.4217	2460345.4228	0.0021	2024-02-04T22:08:52
-b	2460352.5281	2460352.5285	0.0016	2024-02-12T00:41:08
-b	2460373.4251	2460373.4235	0.0019	2024-03-03T22:09:52
-c	2460387.7410	2460387.7379	0.0023	2024-03-18T05:42:40
-b	2460394.3197	2460394.3161	0.0020	2024-03-24T19:35:12
-b	2460415.2182	2460415.2130	0.0022	2024-04-14T17:06:43
-c	2460430.0539	2460430.0478	0.0027	2024-04-29T13:08:54
-b	2460436.1141	2460436.1078	0.0022	2024-05-05T14:35:18
-b	2460457.0139	2460457.0072	0.0024	2024-05-26T12:10:25
-c	2460472.3612	2460472.3547	0.0029	2024-06-10T20:30:48
-b	2460477.9110	2460477.9046	0.0025	2024-06-16T09:42:43
-b	2460498.8116	2460498.8063	0.0026	2024-07-07T07:21:09
-c	2460514.6640	2460514.6598	0.0029	2024-07-23T03:50:14
-b	2460519.7097	2460519.7059	0.0026	2024-07-28T04:56:37
-b	2460540.6109	2460540.6090	0.0027	2024-08-18T02:37:04
-c	2460556.9639	2460556.9636	0.0030	2024-09-03T11:07:42
-b	2460561.5096	2460561.5098	0.0027	2024-09-08T00:14:12
-b	2460582.4109	2460582.4130	0.0027	2024-09-28T21:54:43
-c	2460599.2626	2460599.2659	0.0031	2024-10-15T18:23:00
-b	2460603.3099	2460603.3135	0.0026	2024-10-19T19:31:33
-b	2460624.2107	2460624.2153	0.0026	2024-11-09T17:10:03
-c	2460641.5619	2460641.5667	0.0030	2024-11-27T01:36:11
-b	2460645.1096	2460645.1144	0.0025	2024-11-30T14:44:51
-b	2460666.0095	2460666.0138	0.0024	2024-12-21T12:19:55
-c	2460683.8638	2460683.8671	0.0028	2025-01-08T08:48:45
-b	2460686.9079	2460686.9110	0.0023	2025-01-11T09:51:51
-b	2460707.8064	2460707.8077	0.0022	2025-02-01T07:23:13
-c	2460726.1700	2460726.1696	0.0027	2025-02-19T16:04:14
-b	2460728.7038	2460728.7031	0.0020	2025-02-22T04:52:35
-b	2460749.6007	2460749.5979	0.0019	2025-03-15T02:21:05
-c	2460768.4818	2460768.4774	0.0025	2025-04-02T23:27:29
-b	2460770.4968	2460770.4922	0.0018	2025-04-04T23:48:54
-b	2460791.3917	2460791.3858	0.0016	2025-04-25T21:15:40
-c	2460810.8002	2460810.7937	0.0022	2025-05-15T07:02:56
-b	2460812.2863	2460812.2797	0.0016	2025-05-16T18:42:48
-b	2460833.1792	2460833.1726	0.0015	2025-06-06T16:08:35
-c	2460853.1260	2460853.1201	0.0020	2025-06-26T14:53:01
-b	2460854.0720	2460854.0661	0.0014	2025-06-27T13:35:13
-b	2460874.9628	2460874.9583	0.0013	2025-07-18T10:59:58
-c	2460895.4595	2460895.4566	0.0019	2025-08-07T22:57:37
-b	2460895.8538	2460895.8510	0.0013	2025-08-08T08:25:29
-b	2460916.7427	2460916.7419	0.0012	2025-08-29T05:48:25
-b	2460937.6318	2460937.6330	0.0012	2025-09-19T03:11:37
-c	2460937.8003	2460937.8016	0.0019	2025-09-19T07:14:18
-b	2460958.5189	2460958.5219	0.0012	2025-10-10T00:31:33
-b	2460979.4063	2460979.4105	0.0012	2025-10-30T21:51:10
-c	2460980.1481	2460980.1524	0.0019	2025-10-31T15:39:29
-b	2461000.2918	2461000.2966	0.0011	2025-11-20T19:07:09
-b	2461021.1776	2461021.1822	0.0011	2025-12-11T16:22:29
-c	2461022.5022	2461022.5068	0.0018	2025-12-13T00:09:54

**Notes.** The columns give: the planet name (K2-24, -b or -c), the transit time  $T_0$  predicted by our best-fit dynamical solution (see Section 4 for details) in the JD and BJD-TDB standard along with its  $1-\sigma$  error bar (symmetrized), and the  $T_0$  in the UTC-ISO standard.

**Table A.3.** Transit times of K2-24b and K2-24c predicted by our dynamic model for 2026-2027.

Planet	$T_0$ [JD]	$T_0$ [BJD <sub>TDB</sub> ]	$\sigma(T_0)$ [d]	$T_0$ [UTC]
-b	2461042.0617	2461042.0655	0.0011	2026-01-01T13:34:22
-b	2461062.9461	2461062.9484	0.0011	2026-01-22T10:45:46
-c	2461064.8618	2461064.8639	0.0017	2026-01-24T08:44:05
-b	2461083.8292	2461083.8295	0.0011	2026-02-12T07:54:33
-b	2461104.7125	2461104.7107	0.0010	2026-03-05T05:03:30
-c	2461107.2261	2461107.2242	0.0016	2026-03-07T17:22:51
-b	2461125.5946	2461125.5909	0.0010	2026-03-26T02:10:57
-b	2461146.4770	2461146.4717	0.0010	2026-04-15T23:19:18
-c	2461149.5944	2461149.5889	0.0014	2026-04-19T02:08:05
-b	2461167.3585	2461167.3522	0.0010	2026-05-06T20:27:10
-b	2461188.2402	2461188.2335	0.0010	2026-05-27T17:36:21
-c	2461191.9657	2461191.9590	0.0013	2026-05-31T11:01:02
-b	2461209.1213	2461209.1150	0.0010	2026-06-17T14:45:38
-b	2461230.0026	2461229.9973	0.0010	2026-07-08T11:56:09
-c	2461234.3392	2461234.3342	0.0012	2026-07-12T20:01:18
-b	2461250.8834	2461250.8797	0.0010	2026-07-29T09:06:53
-b	2461271.7645	2461271.7627	0.0010	2026-08-19T06:18:21
-c	2461276.7142	2461276.7129	0.0013	2026-08-24T05:06:40
-b	2461292.6453	2461292.6456	0.0010	2026-09-09T03:29:40
-b	2461313.5263	2461313.5285	0.0010	2026-09-30T00:41:04
-c	2461319.0901	2461319.0927	0.0014	2026-10-05T14:13:34
-b	2461334.4073	2461334.4109	0.0010	2026-10-20T21:51:49
-b	2461355.2884	2461355.2930	0.0010	2026-11-10T19:02:01
-c	2461361.4662	2461361.4710	0.0015	2026-11-16T23:18:18
-b	2461376.1696	2461376.1744	0.0010	2026-12-01T16:11:15
-b	2461397.0510	2461397.0553	0.0010	2026-12-22T13:19:46
-c	2461403.8420	2461403.8460	0.0016	2026-12-29T08:18:18
-b	2461417.9326	2461417.9357	0.0010	2027-01-12T10:27:25
-b	2461438.8145	2461438.8158	0.0010	2027-02-02T07:34:51
-c	2461446.2169	2461446.2175	0.0017	2027-02-09T17:13:15
-b	2461459.6965	2461459.6958	0.0010	2027-02-23T04:42:00
-b	2461480.5790	2461480.5763	0.0010	2027-03-16T01:49:52
-c	2461488.5901	2461488.5866	0.0018	2027-03-24T02:04:50
-b	2461501.4616	2461501.4570	0.0010	2027-04-05T22:58:10
-b	2461522.3448	2461522.3389	0.0010	2027-04-26T20:08:09
-c	2461530.9613	2461530.9550	0.0020	2027-05-05T10:55:20
-b	2461543.2281	2461543.2215	0.0010	2027-05-17T17:19:00
-b	2461564.1122	2461564.1056	0.0010	2027-06-07T14:32:11
-c	2461573.3298	2461573.3235	0.0020	2027-06-16T19:45:50
-b	2461584.9962	2461584.9903	0.0010	2027-06-28T11:46:08
-b	2461605.8813	2461605.8768	0.0010	2027-07-19T09:02:41
-c	2461615.6949	2461615.6912	0.0021	2027-07-29T04:35:24
-b	2461626.7662	2461626.7634	0.0010	2027-08-09T06:19:22
-b	2461647.6525	2461647.6518	0.0010	2027-08-30T03:38:35
-c	2461658.0561	2461658.0564	0.0021	2027-09-09T13:21:14
-b	2461668.5382	2461668.5395	0.0010	2027-09-20T00:56:57
-b	2461689.4259	2461689.4289	0.0011	2027-10-10T22:17:39
-c	2461700.4125	2461700.4162	0.0021	2027-10-21T21:59:27
-b	2461710.3127	2461710.3169	0.0011	2027-10-31T19:36:25
-b	2461731.2017	2461731.2066	0.0012	2027-11-21T16:57:32
-c	2461742.7636	2461742.7684	0.0021	2027-12-03T06:26:33
-b	2461752.0897	2461752.0944	0.0012	2027-12-12T14:15:57

**Notes.** The columns give: the planet name (K2-24, -b or -c), the transit time  $T_0$  predicted by our best-fit dynamical solution (see Section 4 for details) in the JD and BJD-TDB standard along with its  $1-\sigma$  error bar (symmetrized), and the  $T_0$  in the UTC-ISO standard.

**Table A.4.** Transit times of K2-24b and K2-24c predicted by our dynamic model for 2028-2029.

Planet	$T_0$ [JD]	$T_0$ [BJD <sub>TDB</sub> ]	$\sigma(T_0)$ [d]	$T_0$ [UTC]
-b	2461772.9803	2461772.9841	0.0014	2028-01-02T11:37:11
-c	2461785.1086	2461785.1116	0.0023	2028-01-14T14:40:46
-b	2461793.8696	2461793.8718	0.0014	2028-01-23T08:55:28
-b	2461814.7619	2461814.7622	0.0016	2028-02-13T06:17:36
-c	2461827.4473	2461827.4464	0.0024	2028-02-25T22:42:50
-b	2461835.6524	2461835.6506	0.0016	2028-03-05T03:37:00
-b	2461856.5464	2461856.5427	0.0018	2028-03-26T01:01:33
-c	2461869.7792	2461869.7744	0.0026	2028-04-08T06:35:13
-b	2461877.4384	2461877.4331	0.0019	2028-04-15T22:23:42
-b	2461898.3341	2461898.3278	0.0022	2028-05-06T19:52:04
-c	2461912.1041	2461912.0975	0.0029	2028-05-20T14:20:26
-b	2461919.2275	2461919.2208	0.0023	2028-05-27T17:18:04
-b	2461940.1248	2461940.1186	0.0026	2028-06-17T14:50:48
-c	2461954.4222	2461954.4166	0.0033	2028-07-01T21:59:55
-b	2461961.0197	2461961.0144	0.0027	2028-07-08T12:20:52
-b	2461981.9185	2461981.9148	0.0029	2028-07-29T09:57:26
-c	2461996.7340	2461996.7317	0.0038	2028-08-13T05:33:40
-b	2462002.8146	2462002.8129	0.0030	2028-08-19T07:30:41
-b	2462023.7147	2462023.7150	0.0032	2028-09-09T05:09:39
-c	2462039.0403	2462039.0421	0.0041	2028-09-24T13:00:38
-b	2462044.6120	2462044.6142	0.0033	2028-09-30T02:44:32
-b	2462065.5129	2462065.5166	0.0034	2028-10-21T00:23:58
-c	2462081.3425	2462081.3470	0.0043	2028-11-05T20:19:42
-b	2462086.4111	2462086.4158	0.0034	2028-11-10T21:58:46
-b	2462107.3124	2462107.3173	0.0035	2028-12-01T19:36:58
-c	2462123.6419	2462123.6464	0.0044	2028-12-18T03:30:55
-b	2462128.2113	2462128.2156	0.0035	2028-12-22T17:10:30
-b	2462149.1126	2462149.1156	0.0035	2029-01-12T14:46:33
-c	2462165.9405	2462165.9421	0.0044	2029-01-29T10:36:44
-b	2462170.0116	2462170.0129	0.0034	2029-02-02T12:18:42
-b	2462190.9124	2462190.9116	0.0034	2029-02-23T09:52:50
-c	2462208.2399	2462208.2375	0.0044	2029-03-12T17:42:01
-b	2462211.8113	2462211.8085	0.0033	2029-03-16T07:24:17
-b	2462232.7110	2462232.7065	0.0032	2029-04-06T04:57:21
-c	2462250.5422	2462250.5365	0.0042	2029-04-24T00:52:35
-b	2462253.6093	2462253.6034	0.0031	2029-04-27T02:28:59
-b	2462274.5077	2462274.5011	0.0029	2029-05-18T00:01:38
-c	2462292.8490	2462292.8424	0.0038	2029-06-05T08:13:11
-b	2462295.4049	2462295.3984	0.0028	2029-06-07T21:33:46
-b	2462316.3015	2462316.2958	0.0026	2029-06-28T19:05:57
-c	2462335.1617	2462335.1571	0.0034	2029-07-17T15:46:21
-b	2462337.1975	2462337.1930	0.0025	2029-07-19T16:38:00
-b	2462358.0921	2462358.0895	0.0024	2029-08-09T14:08:54
-c	2462377.4813	2462377.4805	0.0030	2029-08-28T23:32:01
-b	2462378.9864	2462378.9858	0.0023	2029-08-30T11:39:35
-b	2462399.8790	2462399.8804	0.0021	2029-09-20T09:07:50
-c	2462419.8083	2462419.8113	0.0027	2029-10-10T07:28:21
-b	2462420.7715	2462420.7746	0.0020	2029-10-11T06:35:31
-b	2462441.6621	2462441.6664	0.0019	2029-11-01T03:59:42
-c	2462462.1429	2462462.1477	0.0026	2029-11-21T15:32:49
-b	2462462.5528	2462462.5576	0.0017	2029-11-22T01:23:03
-b	2462483.4414	2462483.4461	0.0016	2029-12-12T22:42:23

**Notes.** The columns give: the planet name (K2-24, -b or -c), the transit time  $T_0$  predicted by our best-fit dynamical solution (see Section 4 for details) in the JD and BJD-TDB standard along with its  $1-\sigma$  error bar (symmetrized), and the  $T_0$  in the UTC-ISO standard.